

Investigating the Milun Fault: The coseismic surface rupture zone of the 2018/02/06 M_L 6.2 Hualien earthquake, Taiwan

Shao-Yi Huang^{1,*}, Jiun-Yee Yen¹, Bo-Lin Wu¹, I-Chin Yen^{2,3}, and Ray Y. Chuang^{4,5}

¹Department of Natural Resources and Environmental Studies, National Dong Hwa University, Hualien County, Taiwan

²Graduate Institute of Applied Geology, National Central University, Taoyuan City, Taiwan

³YIC Geological Office, Penghu County, Taiwan

⁴Department of Geography, National Taiwan University, Taipei City, Taiwan

⁵Research Center for Future Earth, National Taiwan University, Taipei City, Taiwan

Article history:

Received 17 July 2018

Revised 29 November 2018

Accepted 9 December 2018

Keywords:

2018 Hualien earthquake, Milun Fault, Sinistral strike-slip fault, Surface rupture zone, Step-over

Citation:

Huang, S.-Y., J.-Y. Yen, B.-L. Wu, I.-C. Yen, and R. Y. Chuang, 2019: Investigating the Milun Fault: The coseismic surface rupture zone of the 2018/02/06 M_L 6.2 Hualien earthquake, Taiwan. *Terr. Atmos. Ocean. Sci.*, 30, 311-335, doi: 10.3319/TAO.2018.12.09.03

ABSTRACT

On 6 February 2018, a M_L 6.2 earthquake struck the east coast of Taiwan and caused more than 200 casualties in the Hualien area. The mainshock initiated at a shallow depth of 6.3 km and was accompanied by numbers of foreshocks and aftershocks. Coseismic ruptures widely occurred along the Milun Fault with various deformational structures and caused a variety of damage. Extensive field survey and drone-based images reveal the distribution of offsets and the characteristics of the surface ruptures. The major surface ruptures were mostly synthetic and antithetic Riedel shears interlinked by push-up moletracks or tensional fissures. The strike of the principal displacement zone evolved from northeast to northwest and defined a 7.5-km-long NS fault trace concave to the east. The vertical offset reached its maximum of 50 cm on the north segment and became insignificant toward south. Both on-fault single measurements and cumulative sinistral offsets estimated across the rupture zones showed the pattern of southward declining with the maximum offset of 77 cm in the north. The width of the damage zone increased from 1 - 20 m to maximum 270 m in the south where the overstepping segments occurred. The development of step-overs is significant in the south, especially in the downtown area where slip is distributed across a transpressional area. Overall, the distinct features of the coseismic ruptures reflect the complex near-surface geology along the Milun Fault and offer new insights for future hazard assessments of the Hualien area.

1. INTRODUCTION

1.1 The 2018 Hualien Earthquake

The 2018/02/06 M_L 6.2 Hualien earthquake struck the nearshore of Hualien at 23:50 local time with a shallow hypocenter depth of about 6.3 km, causing a high I_{CWB} of 7 in the middle of Hualien City, and generated surface ruptures along the Milun and the northern most part of the Lingding Faults (CWB 2018; Fig. 1a). The shock immediately resulted in the collapse and toppling of four buildings in downtown Hualien and caused massive outages of power and water for days. The death toll reached 17 and there were more than 200 people injured mainly due to the associated damage along the Milun Fault (Fig. 1b). Focal

mechanisms derived two possible nodal planes: one strikes 216° with a dip of 56° and the other one strikes 111° with a dip of 69° (CWB 2018). This earthquake was accompanied by one foreshock and many aftershocks with magnitude larger than 5. The aftershock sequence showed a tendency of clustering over a northeast-striking structure extending towards on-land with mostly normal faulting mechanisms on steep west-dipping nodal planes (Kuo-Chen et al. 2018). However, the on-land coseismic damage concentrated along the Milun and the Lingding Faults, which are 13 - 23 km south of the nearshore epicenter and both are previously documented as left-lateral reverse faults dipping to the east (Yang 1953; Hsu 1962; Shyu et al. 2016b).

The contradiction between the west-dipping moment

* Corresponding author
E-mail: Shao.syh@gmail.com

tensor solutions and the east-dipping surface structures raised a challenging question of how to unveil the connection between the seismogenic origin imaged at depth and the ruptured fault systems on the surface. The passive role of the Milun Fault in the 2018/02/06 earthquake is suggested by the latest studies from the seismic analysis, InSAR images and GPS displacement with diverse perspectives of kinematic models. Based on the results of joint source inversion, Lee et al. (2018) suggest that the rupture started from the west-dipping fault plane in the north and propagated to the south, triggering the slip on the Milun Fault and then the Lingding Fault. Yang et al. (2018) proposed that the ruptures of the Milun Fault and an unknown west-dipping fault were triggered by a west-dipping seismogenic fault from the north with the faulting models using InSAR and GPS results while the Lingding Fault is not emphasized in their model. Given the discrepancies of different models, a general interpretation is that the slip on the Milun Fault was triggered from the seismogenic fault in the north and propagated towards the south.

1.2 The Milun Fault and 1951 Longitudinal Valley Fault Earthquake

The Hualien area is recognized as a transition zone

of two subduction systems (Suppe 1984; Barrier and Angelier 1986; Malavieille et al. 2002). To the northeast of Taiwan, the Philippine Sea Plate is subducting beneath the Eurasian Plate along the Ryukyu Trench and to the south, the Eurasian Plate is subducting under the Philippine Sea Plate along the Manila Trench. Located at the northern tip of the Longitudinal Valley, Hualien City sits on Holocene alluvial deposits, mainly transported by rivers draining the east flank of the Central Range. To the west of the Longitudinal Valley, the Central Range displays a sudden increase of relief up to a few thousand meters high, comprising a severely deformed metamorphic complex which represents the continental margin of the Eurasian Plate. On the other hand, to the southeast of Hualien City, the Coastal Range comprises the material of the Luzon Arc, representing the remnants of the Philippine Sea Plate. Although the connections with the deep architecture remain unclear, several possible active structures have been proposed around Hualien City, mostly based on their prominent geomorphic features (Fig. 1c). These proposed structures include the Milun Fault (Lin and Hsiao 1998; Yamaguchi and Ota 2004; CGS 2010; Shyu et al. 2016b), the predominant NS structure following the western edge of the late Quaternary uplifted marine terrace (up to 100 m at the Mt. Milun); the northeast-striking strike-slip faults of the Minyi Fault (Lin and Hsiao 1998;

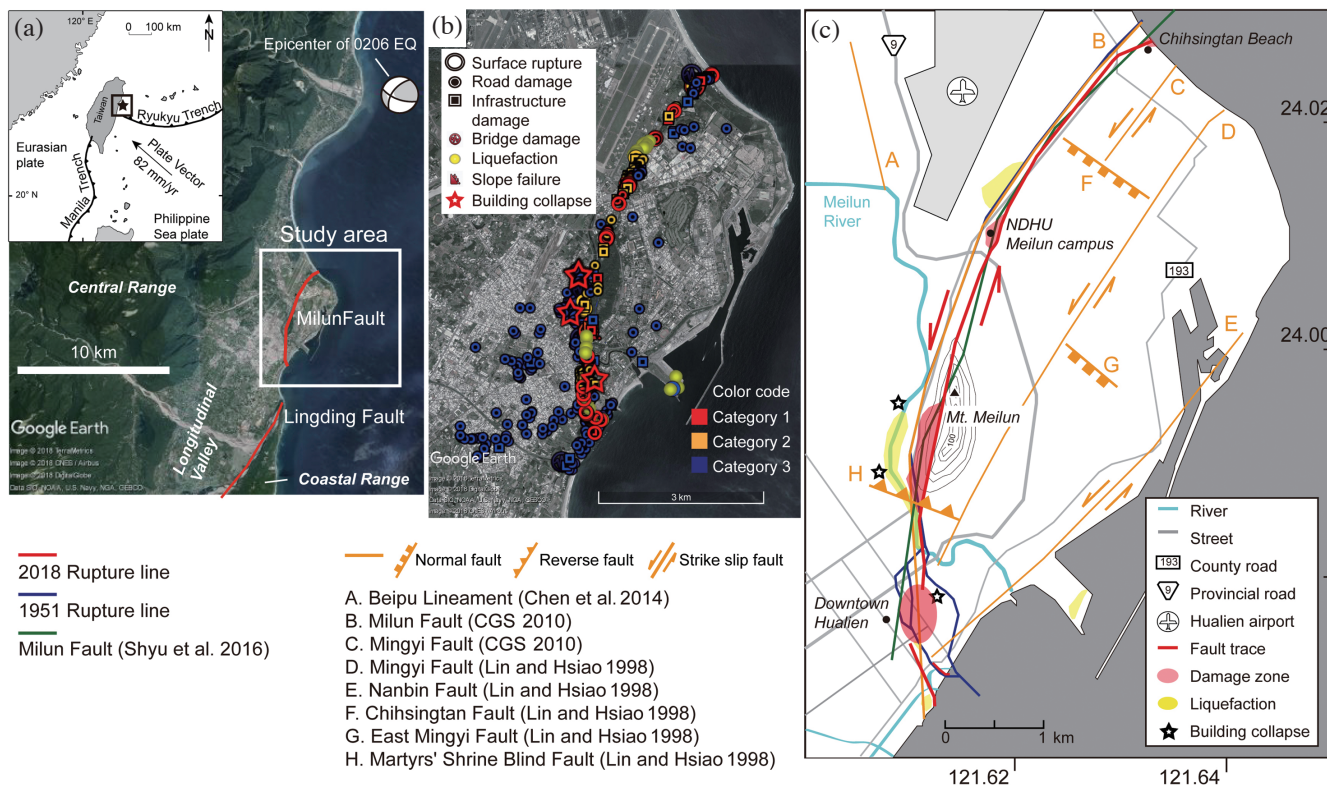


Fig. 1. Index maps. (a) The regional map of the study area. The epicenter and focal mechanism of the 0206 earthquake are presented. (b) Damage points and rupture lines are color-coded as: red (category 1), yellow (category 2), and blue (category 3) with different damage types shown in the legend. (c) Schematic map of the 2018 fault trace and the surrounding structures. The 1951 fault trace is modified from CGS (2010).

CGS 2010; Yen et al. 2011) and the Nanbin Fault (Lin and Hsiao 1998); the northwest-striking normal faults of the Chihsingtang Fault (Lin and Hsiao 1998) and the East Minyi Fault (Lin and Hsiao 1998; Chen et al. 2014); the northwest-striking topographic high of the Beipu structure (Chen et al. 2014); and to the southeast, the Lingding Fault which bounds the western side of the Coastal Range (CGS 2010). Among these structures, the Milun Fault is the only earthquake fault with documented fault displacement of the 1951 Longitudinal Valley Fault earthquake (Yang 1953; Hsu 1962; Bonilla 1975, 1977; Cheng et al. 1999) and thus is categorized as a Holocene active fault by CGS.

The 1951 Longitudinal Valley Fault earthquake is a devastating earthquake sequence that resulted in over 80 fatalities and destroyed numerous houses. The earthquake sequence includes three magnitude 7 events on the north end of the Longitudinal Valley on 22 October and two earthquakes larger than magnitude 6 on 25 November. The October group of earthquakes generated ruptures of ca. 15 km long at the northern end of the valley (Hsu 1962). For the purpose of this study, the 1951 earthquake in the context mainly refers to the October sequence hereinafter. The maximum displacements of the 1951 earthquake were reported as 2 m sinistral offset and 1.2 m uplift along the Milun Fault (Yang 1953; Hsu 1962; Cheng et al. 1999). Shyu et al. (2016b) estimated the slip rate of the Milun Fault to be around 10 mm yr⁻¹ with a recurrence interval of 70 yr and an average displacement of 0.68 m per event.

Although there are abundant photographs documenting surface damage during the 1951 earthquake, the exact locations of the ruptures are still ambiguous due to the absence of coordinate records. As Shyu et al. (2007) mentioned, the ambiguity of the historic records may lower our confidence on further interpretations. For instance, the location of the max. 2 m sinistral offset is described as 7 km northeast of Hualien City, which in fact attributes the surface damage to the Mingyi Fault (Chu and Yu 1997; Lin and Hsiao 1998; Cheng et al. 1999; Fig. 1c). The 1951 fault trace was illustrated as three segments as the fault extended into the old Hualien City according to the archived photos and newspapers (Chu and Yu 1997; Lin et al. 2009). It is still questionable how the three segments connected as most of the photos only showed massive toppling and collapse of houses rather than validated surface ruptures. It is possible that the proposed fault segments may only represent the envelope area of the damage zone.

1.3 Aim of This Study

Although the Milun Fault is identified as an active fault with high seismogenic potential and has rupture records of the 1951 earthquake, there are still a lot of uncertainties on the location and extension of the fault. The 2018 Hualien earthquake provides the opportunity to revisit the on-land

trace of the Milun Fault and establish a detailed database of rupture locations, rupture behaviours, amount of offsets, and extent of the fault with the help from high-precision GPS devices and high-resolution drone images. The aim of this study is to provide a comprehensive dataset that compiles a vast number of on-site measurements and photos to reveal the characteristics of the Milun Fault and to facilitate further analyses.

2. METHODOLOGY

2.1 Strategy

Field survey of surface damage has continued since the day after the late night earthquake. Measurements of strike, rupture length, offset amount, and damage type were recorded on-site with compass and tape measures. Some sites with complex rupture behaviours were checked with real-time kinematic (RTK) GPS. Aerial photos taken with Unmanned Aerial Vehicle (UAV) by the National Land Surveying and Mapping Center (NLSC), the Eastern Taiwan Earthquake Research Center (ETEC), and the group of National Dong Hwa University were investigated and processed to provide orthomosaic photos for rupture identification.

In this article, we report 565 points of damage records and map traceable surface rupture lines associated with the 2018 Hualien earthquake. The kml file, detailed measurements and coordinates of the damage records are presented in the supplementary data. In order to provide an accessible dataset for public use, all of the reported coordinates (latitude and longitude) use World Geodetic System (WGS84) as their reference coordinate system and can be directly projected with Google Earth. The layout of our index maps also adopted street maps from Google Earth for the purpose of visually showing how the damage zones passed through the densely populated downtown Hualien.

2.2 Terminology

In the following context, the term “*surface rupture line*” stands for the traceable, coseismic surface deformation of the 2018 Hualien earthquake, including the forms of tensional cracks, Riedel shears, restraining moletracks, buckled pressure ridges, and damage on artificial infrastructures (e.g., buildings, walls, floor tiles, pavements, tarred roads and so forth). Although most of the coseismic rupture lines are discontinued in length of only several meters and did not develop a through-going fault trace, the extension of the fault can still be well defined by the occurrence of the *principal displacement zone* (PDZ). In this article, “*fault trace*” is defined by the continuous trace of PDZ resulting from the faulting of the 2018 Hualien earthquake (Fig. 1c).

In the records, *damage types* are classified as simple surface rupture, road damage, infrastructure damage, liquefaction, and slope failure according to the nature of reported

survey points. *Damage form* reports the moving sense of deformed blocks as sinistral sense, dextral sense, uplift (reverse), subsidence, compression, tension, and collapse. The amount of offsets are recorded accordingly with respect to their damage forms wherever measurements can be taken. Orientation of strike is recorded with quadrant format (e.g., N35°E) so that it is easier to visualize how the rupture lines compare to the regional structures.

The 565 survey points were classified into three levels: Category 1 includes surface ruptures that can be directly identified as the major ruptures related to the slip surface. These damage points can occur as the type of opening cracks or surface offset on the bare ground such as the enechelon shears or the fault scarp, the ruptures on tarred road or polyurethane tracks, or the offset or fissures in any given infrastructure such as a building, wall, fence, or pavement. The main goal of the category 1 point is to recognize the main slip zone where most of the displacement was accommodated.

Category 2 includes surface deformation that occur outside of the fault core and display relatively lower strain and less intense shearing. These damage points refer to the secondary structures such as arrays of subsidiary ruptures, single or conjugate shears on the ground or in any given infrastructure. The category 2 points display varied surface deforma-

tion in a wider damage zone rather than within the highly localized fault core and often occur as the moletracks, pressure ridges, and shears with small to undetectable offsets. Category 3 corresponds to damage that occurs as a response to the strong ground motion and is not directly related to the movement of the fault. These damage includes the type of the slumping along the riverbank, the fissures or breakdown of any given infrastructures. Category 3 points can occur not only inside the main damage zone but also in a wider range because they mainly represent the strength and competence of the material.

The distribution width of Category 1 and 2 points therefore represent the *main damage zone* (MDZ), where most of the slip is released and presented as the surface ruptures or associated damage types. MDZ depicts the range of the localized fault core (Category 1) and the wide damage zone (Category 2). On the other hand, the extension of Category 3 points defines the width of the *secondary damage zone* (SDZ), which relates more to the competence of the construction material and the engineering strength than the tectonic significance. The use of descriptive terms on the damage zones and the segments in this study are illustrated in Fig. 2: due to the characteristic of the segmented sinistral fault, in this study we mainly discuss the along-fault damage zones of the wall damage zones (the wall of the fault

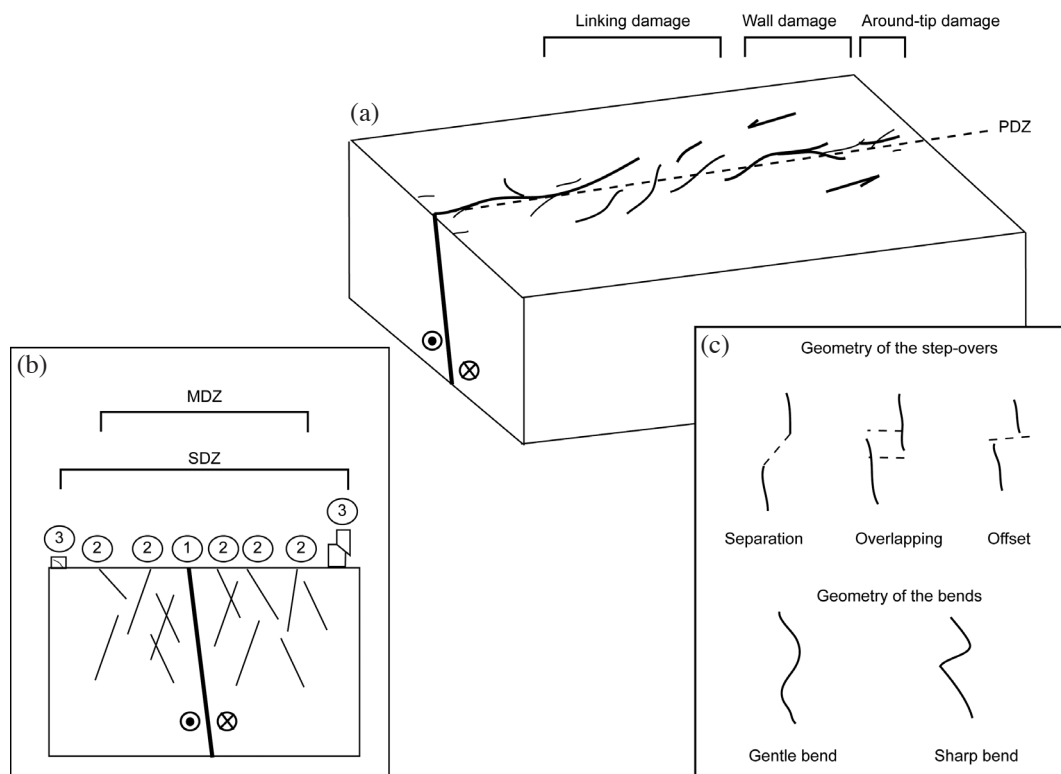


Fig. 2. The descriptive term of the damage zones and the fault segments. (a) The schematic block diagram showing the along-fault damage zones of a segmented sinistral fault. The linking damage zone (areas with bifurcated segments), wall damage zone (areas with mostly single fault trace), and around-tip damage zones (area at the tip of the segments) are presented. (b) A schematic cross section showing the cross-fault damage zone and the range of MDZ and SDZ. (c) The possible linkages of the fault segments.

trace), the linking damage zones (areas with the bifurcated segments), and the around-tip damage zones (damage structures at the end of the fault trace); MDZ and SDZ are incorporated in the discussion of the cross-fault damage zone (Choi et al. 2016).

3. SURFACE RUPTURES OF THE MILUN FAULT

Like many other strike-slip faults around the world, the coseismic surface rupture of the Milun Fault did not generate a simple, co-planar fault trace (Segall and Pollard 1980; Aviles et al. 1987; Scholz 1990; Sylvester 1988; McClay and Bonora 2001; Klinger 2010). The surface deformation mostly occurred as arrays of en-echelon arranged Riedel shears (mainly R), tension fissures and buckled moletracks synthetic to the direction of PDZ (Tchalenko 1970; Davis et al. 2000; Chemenda et al. 2016). Antithetic R' shears also occurred occasionally but overall appeared to be less prominent than the R shears. Although the ruptures arrested and bifurcated as many segments before developed into a through-going fault, the extension of PDZ were very clear and continuous, allowing us to map out the surface damage zone of the fault on-land in the length of ca. 7.5 km. Along the 7.5-km fault trace, we choose here 24 main sites (labelled as A to W) to display the representative rupture features of the fault. In this section, we will go through the surface ruptures from north to south, explaining the location, orientation, and field features of the investigated damage zones.

3.1 Chihsingtang Beach

The northernmost rupture on-land occurred at the Chihsingtang Beach area (Fig. 3a) where two parallel lineaments of fault trace were observed on the gravel beach with a 30-cm-sinistral (site A1, Fig. 4a) and a 20-cm-uplift (site A2, Fig. 4b) offset, respectively. The dipping direction of the fault plane can be observed to east but the actual angle is hard to estimate because of the unconsolidated nature of gravel beach.

The ruptures in this area in general followed the strike of N60°E and extended southwestward from the beach. On the tarred parking lot adjacent to the beach, the fault generated arrays of both synthetic (10- to 30-cm-sinistral offset) and antithetic (10- to 50-cm-dextral offset) Riedel shears (site B, Fig. 4c). These shear also displayed vertical offsets along their sigmoidal ends, showing the component of dip slip. The maximum sinistral offset was observed as the fault ran into the houses of Chihsing Street (site C1, Fig. 4d) next to the parking lot. The rupture passed in between the houses, inducing a maximum 77-cm-sinistral offset and at least 40-cm-uplift on the upthrown side (east of the fault trace), and consequently caused the tilt of the houses at site C2. The row of the tilted houses were pushed northwest, which

resulted in 80-cm-compression in front of the houses (site C2-front; point 15; Fig. 4e). The preliminary report from CGS (2018) estimated the amount of vertical offset to be 80 cm according to the shortening features. However, we suspect that the vertical slip in this area should be smaller as we can trace the rupture from C1 all the way through the back of the houses (site C2-back; point 565) and an apparent 27-cm-uplift of the floor base was recorded at one of the tilted houses when the repairing team attempted to excavate the base of the tilted building and lift the floor back to level with arrays of hydraulic lifting jacks. The thrust surface rupture lifted the rear corner of the house and caused the front corner of the building to push against the tarred road, resulting prominent compressional damage along the front of the houses. The net vertical offset near site C2 therefore should be in the range of 20 (max. amount at site A) to 40 (max. amount at site C1) cm and we identified the 80-cm-compression as the category 3 damage which is not directly referred as the surface rupture (Fig. 3a).

As the fault extended southwest into the hill of Mt. Chihsing, the revetment was damaged and showed an opening of over 40 cm along the fault trace (site D). The rupture remained N60°E-striking and displayed an offset of 70-cm-sinistral at the margin of the hiking trail (site E1, Fig. 4f) and at least 30 cm of compression at the trail nearby (site E2, Fig. 4g) before it passed through the Chihsingtang Bridge. The southern end of the bridge was severely damaged with disrupted concrete blocks moving along the sheared senses (site F, Fig. 4h) and at least 70 cm of sinistral offset was estimated by CGS (2018).

3.2 North Meilun

South of the Chihsingtang Bridge, the rupture developed on the slope of a pre-existing scarp with the strike of N37°E (Fig. 3b) and produced comparable amount of uplift (ca. 50 cm of the east side) and cumulative sinistral offset (ca. 70 cm) as in the Chihsingtang Beach area (site G, Fig. 5a). Further south, abundant liquefaction features occurred (site H, Fig. 5b) over a wide range of area (400 by 100 m) that used to be a swamp area and the PDZ started to occur on the east side of Huashi street as several northwest-striking shears formed and produced tensional and sinistral offsets across the street (site I).

To the south, as the fault extended into the campus of National Dong Hwa University, the rupture bifurcated into two segments: sites J1 and J2 (Fig. 3c). The representative ruptures of J1 comprised northwest-striking shears with max. 7-cm-sinistral and 3-cm-dextral offsets arranged as en-echelon arrays on the polyurethane running tracks (Figs. 5c and d). Rupture segments in this area typically arrested in limited length of 2 - 10 m. The representative rupture features of J2 consisted of Riedel shears and push-up moletracks that connected the associated shears and

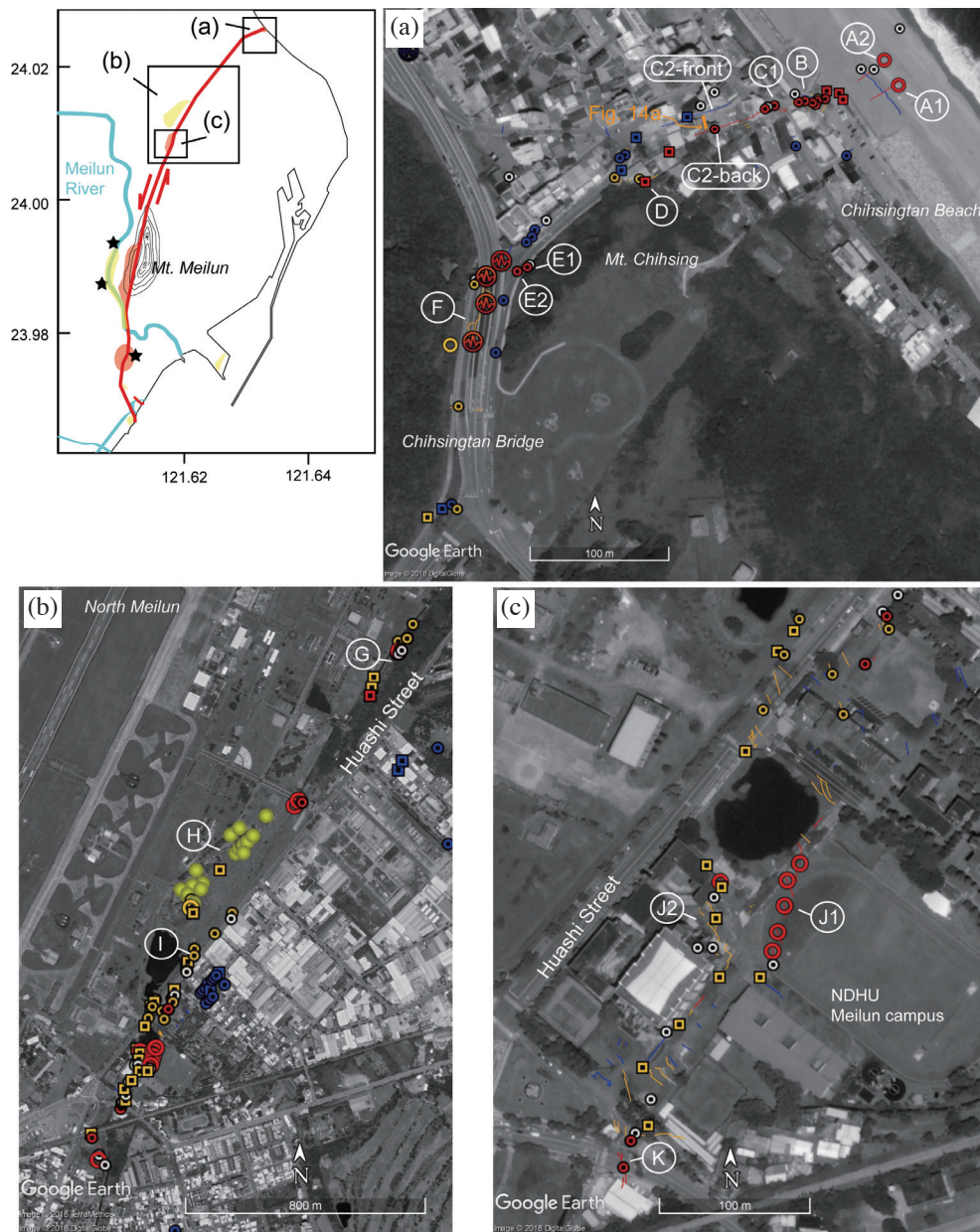


Fig. 3. Maps showing damage points in the north segments. (a) Damage points in the Chihsingtan Beach area. The location of the excavation is labelled (Fig. 14a). (b) Damage points in the north Meilun area. (c) Close-up map showing damage points and rupture lines in the campus of NDHU.

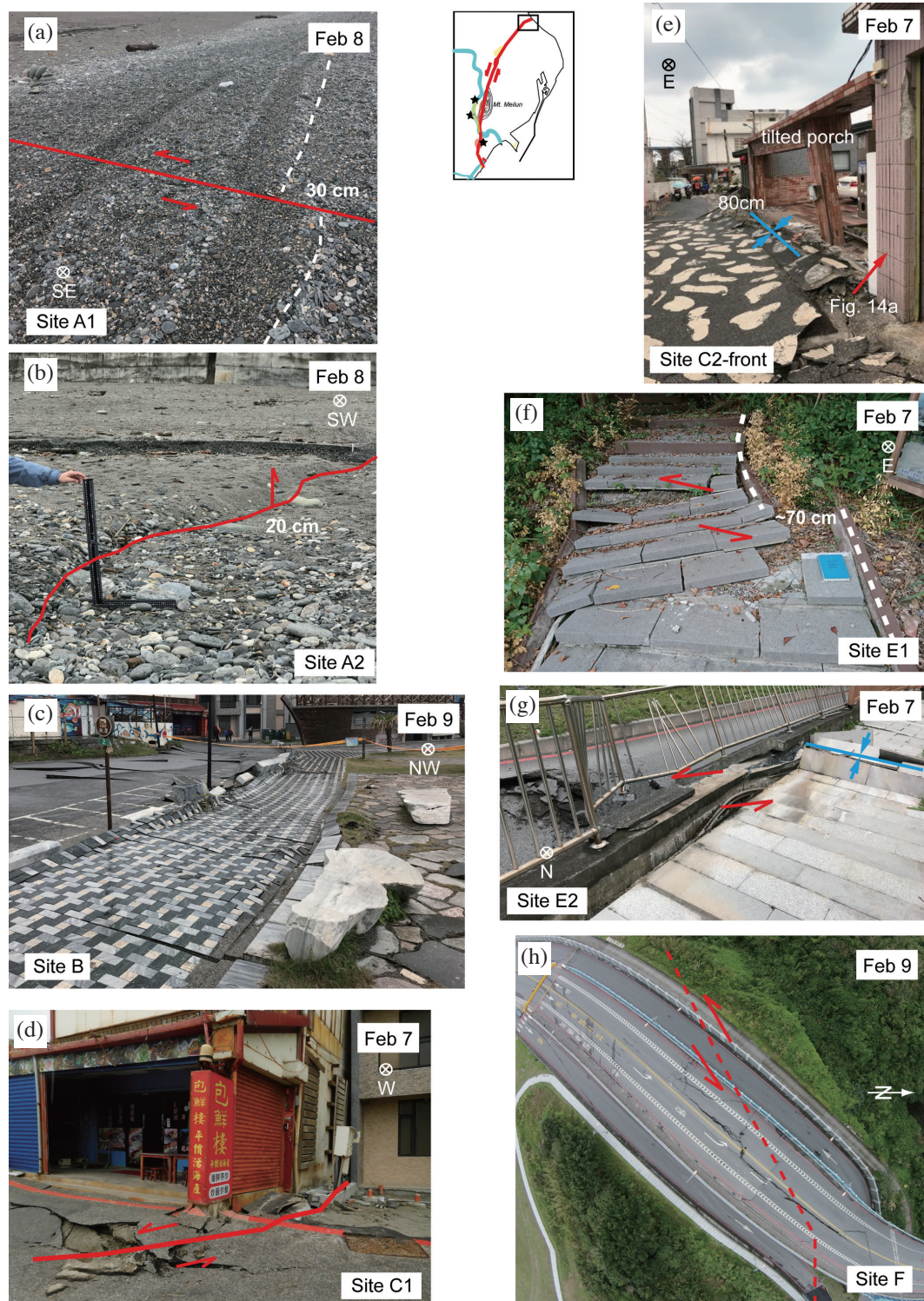


Fig. 4. Field photos of the representative ruptures. (a) Offset wheel track on the gravel beach. (b) Uplifted scarp on the beach. (c) Drone image of the Chihsingtan Parking Lot, showing a series of Riedel shears and en-echelon folding. (d) Surface rupture that ran across the houses and caused sinistral and reverse offsets. (e) Compression along the tarred road and the tilted porch pushing forward against the road. (f) 70-cm-sinistral offset passed through the hiking trail. (g) Sinistral offset ran across the trail and continued to the road below. (h) Drone image over the Chihsingtan Bridge showing massive ruptures on the bridge.

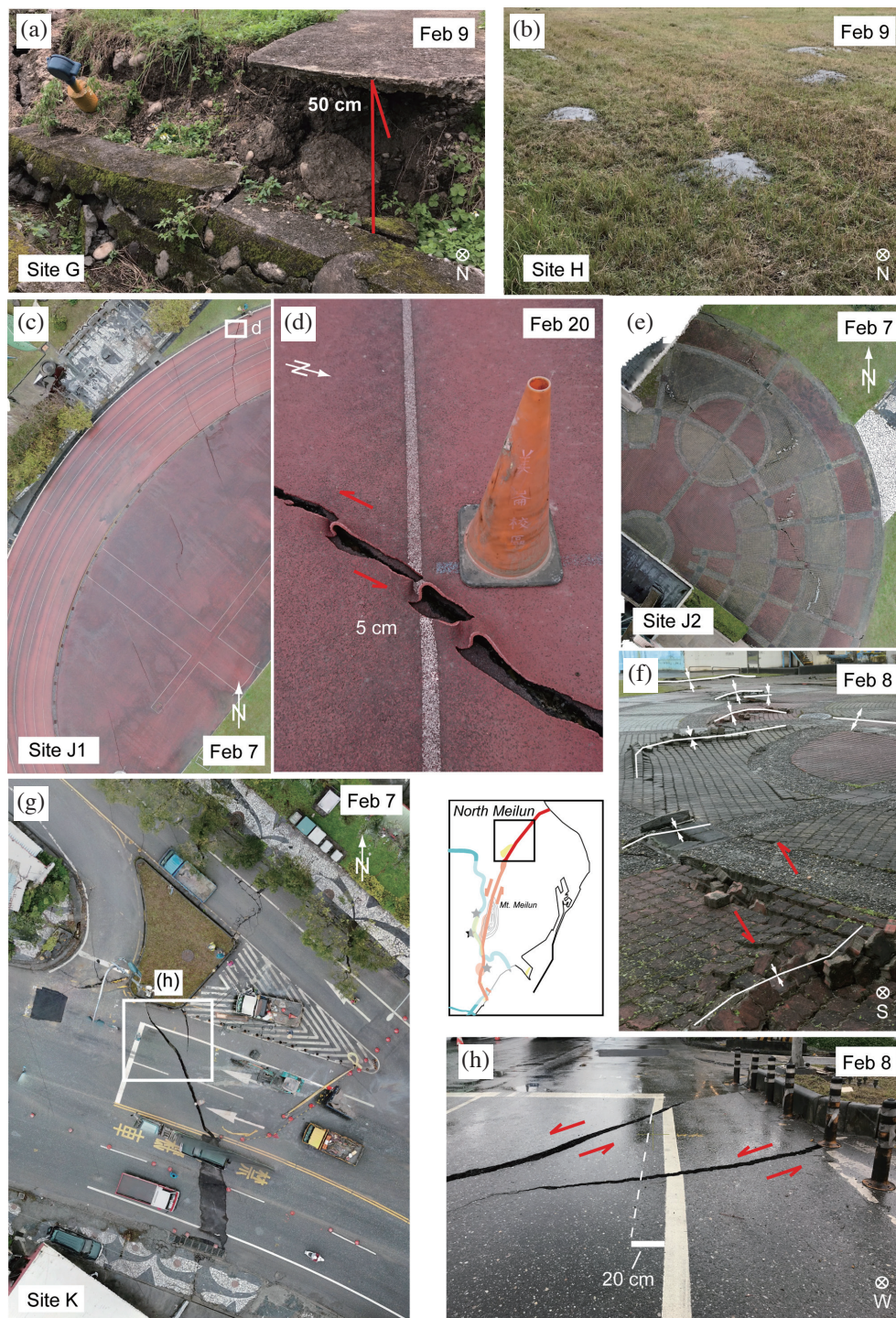


Fig. 5. Field photos of the representative ruptures. (a) Uplifted pavement. (b) Liquefaction features in area of site H. (c) Drone image over the track field of the campus, NDHU, showing a series of Riedel shears. (d) One of the shears showed a 7-cm-sinistral offset. (e) Drone image over the Meilun campus of NDHU, showing the development of shears and restraining bends. (f) Close-up of the push-up moletracks that connected the shears. (g) Drone image showing the multiple offsets south of the NDHU Meilun campus. (h) The road mark was offset about 20 cm in total.

tensional fissures (Figs. 5e and f). Compared with J1, the surface deformation zone at J2 was more continuous and possibly reflected the strength of overlying material as the brick tiles were easier to disrupt than the polyurethane running tracks. Most of the deformation at J2 was accommodated as push-up features and thus added more uncertainties on the estimated amount of offsets. Hsu et al. (2018) have evaluated the total amount of surface offset at J2 to be around 15 cm sinistral.

The two segments converged back to one as the fault trace extended towards south and disrupted the roads south of the campus (site K, Figs. 5g and h). On-site measurement and RTK GPS survey of the damaged tarred roads showed clear sinistral displacement of 20 - 30 cm. It is to note that the amount of vertical offset has significantly waned from south of sites I to K.

3.3 Mt. Meilun

The trace of earthquake faulting can be tracked further south with a general strike of $N24^\circ E$ until the hill of Mt. Meilun. At site L (Fig. 6), sinistral cracks with max. 6-cm-tension occurred on the peanut field and extended southward as en-echelon arrays (Fig. 7a). These tensional shears generally arrested in short length (ca. 2 - 18 m) and the amount of sinistral offset is not significant on each trace. CGS estimated the total sinistral offset here to be more than 30 cm according to the disrupted ditch nearby (CGS 2018).

The fault ruptures observed in the Mt. Meilun area can be divided into three groups (Fig. 6): site M represents the main direction of PDZ across the mountain (around $N10^\circ E$); site N represents the western margin of Mt. Meilun where varied surface damage were reported; site O represents the south bank of the Meilun River where plentiful tensional cracks, liquefaction, and slope failures occurred.

The rupture appeared on the west flank of Mt. Meilun at the intersection of Shangzhi Rd. and Xinxing St. and produced a max. 15-cm-sinistral offset with S-shaped moletracks on the tarred road (site M1, Fig. 7b). The surface damage can be traced southward as a series of northwest-striking en-echelon tensional shears on the bare ground of a banana field within a total length of ca. 90 m (site M2, Fig. 7c). Most of the tensional shears were about 2 m long (max. 20 m) and displayed opening of 1 - 20 cm. The fault trace ran across the Shangzhi Water Purification Plant and extended southward to the hillside of Mt. Meilun (site M3, Fig. 7d). The rupture can be continuously traced until the southern tip of Mt. Meilun. At site M4 (Fig. 7e), the surface rupture cut through a meadow, causing the tilt of streetlight pole, the toppling of the bushes, and an offset of 2-cm-sinistral of the pavement bricks. Prolonged surface deformation such as tensional fissures and Riedel shears can be observed across the Martyrs' Shrine (site M5, Fig. 7f).

Away from the hillslope, site N included the western margin of Mt. Meilun and consisted of a series of restraining deformation such as buckled and S-shaped moletracks

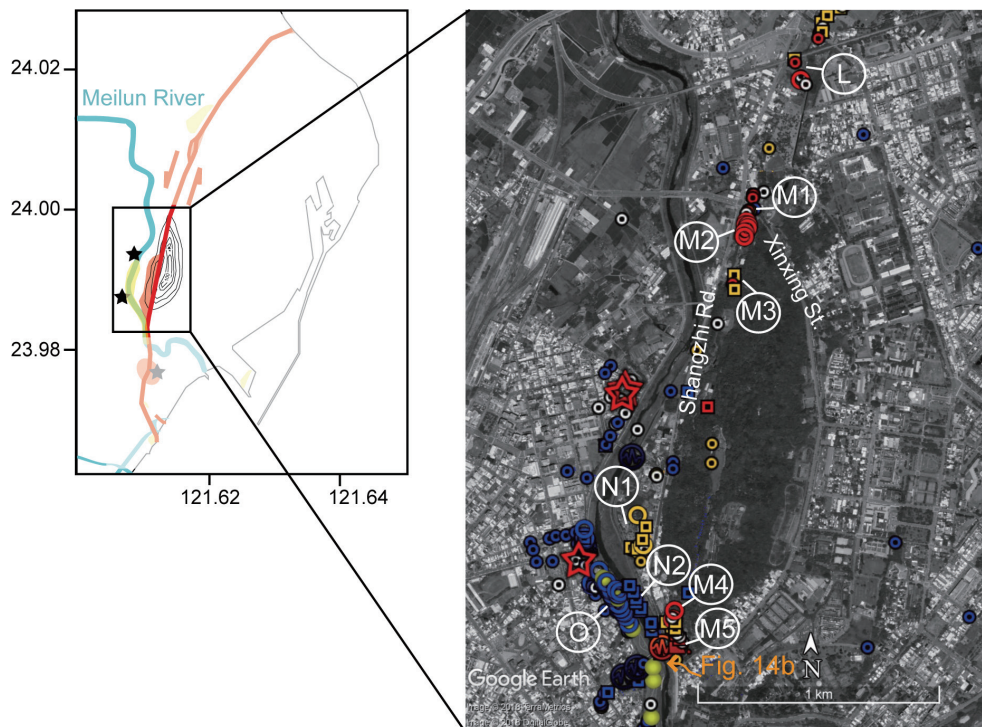


Fig. 6. Close-up maps showing the damage points in the Mt. Meilun area.

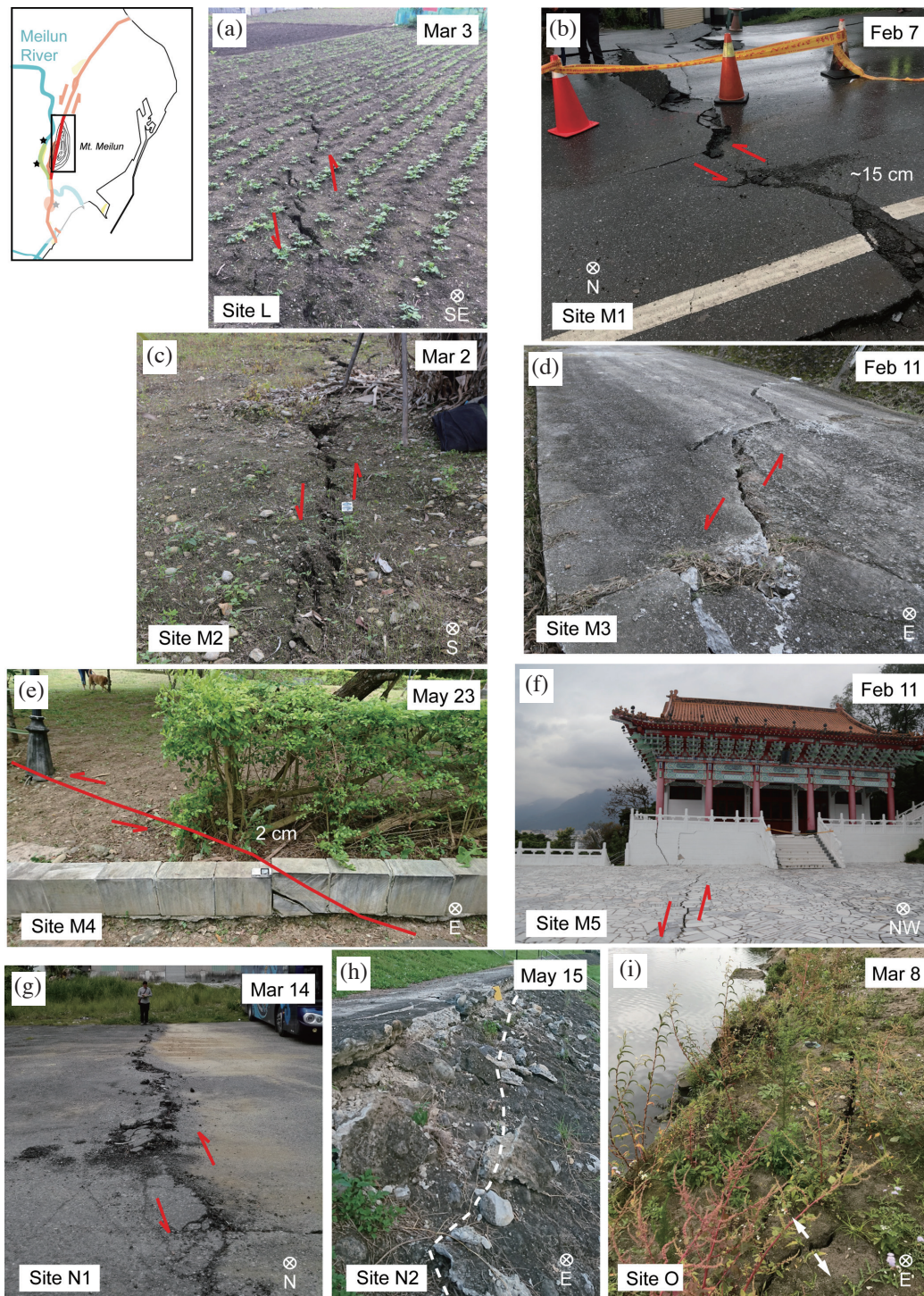


Fig. 7. Field photos of the representative ruptures. (a) En-echelon cracks on the peanut field. (b) The road mark was ruptured about 15 cm with S-shaped moletracks. (c) En-echelon cracks on the banana field. (d) Sinistral offset on the concrete road of Shanzhi Water Purification Plant. (e) Sinistral offset passed through the streetlight, bushes, and the bricks, causing the toppling of the bush and the bricks. (f) Sinistral shears ran across the Martyr's Shrine. (g) S-shaped moletracks with sinistral component passed through the parking lot of site N1. (h) The revetment was continuously damaged along the north bank of Meilun River. (i) Surface cracks parallel to the river occurred along the south bank of Meilun River.

along the gutters and the field (site N1, Fig. 7g). Pull-apart depressions occurred locally with up to 50 cm subsidence and appeared to be related to poor compaction of foundations rather than tectonic offset. The surface deformation extended to the north bank of the Meilun River and resulted in significant damage on the embankment (site N2, Fig. 7h) in the forms of sinistral and dextral shears, push-up ridges, and collapse of dike walls and pavements. The south bank of the river featured a great number of liquefaction features and tensional cracks (site O, Fig. 7i). However, these surface openings mostly were parallel to the river course and appeared to be rather related to the slumping of river bank deposits. In general, site O comprised very few infrastructure damage when compared with the north bank, reflecting its poor connections with PDZ. The main rupture ran through site M and extended to the north end of the Shanzhi Bridge before passed the Meilun River.

3.4 Downtown Hualien

The ruptures extended into the downtown area and displayed a more complex distribution (Figs. 8a and b). At the south bank of Meilun River, the rupture occurred as tensional cracks north of the Mingli elementary school (site P1, Fig. 9a) and generated northwest-striking shears and a prominent E-W striking push-up ridge inside the campus (site P2, Fig. 9b). The surface rupture passed through the campus and extended south into the city. The ruptures in the downtown area were no longer restricted in a width of couple meters as in the north segments. Instead, a series of northwest-striking ruptures occurred in a broad width of ca. 270 m as an array of fully or partially overlapping lineaments (sites Q to S). These ruptures caused continuous damage on the buildings, roads, and infrastructures and can be tracked easily. For instance, sites Q1 and Q2 clearly displayed the occurrence of PDZ, breaking through the front (Fig. 9c) and back (Fig. 9d) doors of a kindergarten. The amount of offset near Q1 was measured from the shifted poles on the street with RTK GPS to be around 10-cm-sinistral. Sites Q3 and Q4 both presented 5-cm-sinistral offsets (Figs. 9e and f). Push-up ridges also occurred at site Q5 (Fig. 9g) with a northeast strike and a compressional amount of around 10 cm. The cumulative amount of total offsets in the area of site Q thus were estimated as 10 - 15 cm.

The surface ruptures passed through site R and resulted in the toppling of stone plates and pavement bricks (Fig. 9h). Distributed offsets were also recorded at site S where several prolonged sinistral ruptures occurred across the Hualien Railway Culture Park Hall 2 (site S1, Fig. 10a) and Hall 1 (site S2, Fig. 10b). The PDZ advanced further south from Hall 2, producing multiple rupture lines with ~10-cm-sinistral offset at site T1 (Fig. 10c) and generated a series of northwest-striking en-echelon tensional shears connected by northeast-striking push-up moletracks on the

tarred field (site T2, Fig. 10d). The rupture zone can be continuously tracked across the street into the night market area with prominent tensional cracks and a gentle scarp of ~15 cm uplift (e.g., site U2, Fig. 10e), a series of push-up ridges and en-echelon fissures (e.g., site U3, Figs. 10f and g), and occasionally liquefaction features (site U4, Fig. 10h).

The PDZ marched forward south with two rupture zones: the minor one occurred to the southeast of the night market and generated several prolonged ruptures that cut across the street and the Funeral Parlour before extending into the coastal line (site V2, Fig. 10i). The major one advanced southward directly (site W, Fig. 11a) and broke through the Water Pumping Station (site W2, Fig. 11b) and the channel (site W3, Fig. 11c). At site W2, the rupture produced 3-cm-sinistral offset on the concrete wall (Fig. 11b1) and opened at least two fissures on the revetment of the Water Pumping Station (Fig. 11b2). The ruptures proceeded toward the coast, passing through the artificial channel (Fig. 11c1) and caused several tensional cracks on the surface of the hillslope (Fig. 11c2). The surface ruptures continued across the tarred trail and then became obscured on the gravel beach.

4. DISCUSSION

The surface ruptures of the 2018 Hualien Earthquake occurred as various forms with distributed deformation along the fault. In the following sections, we will discuss how the geometry of the fault trace and the amount of offsets evolve along the strike of the fault; how the segmented fault developed as step-overs with distributed deformation; how the on-site measurements of offsets differ from the estimates acquired from the remote sensing tools and its seismotectonic implications; and last but not least, how the 2018 surface ruptures coincide with historical records and paleoseismological evidence.

4.1 Field Characteristics of the 2018 Surface Ruptures

The surface ruptures of the Milun Fault displayed a variety of deformation forms, mainly Riedel shears with synthetic and antithetic sense to the direction of PDZ connected by associated tension cracks or push-up ridges. In general, R shears and tension cracks developed with count-clockwise angles to PDZ and the restraining structures occurred with clockwise angles. Field mapping of the rupture lines confirmed the change of fault strike from north to south and the corresponding evolution of the relevant Riedel shears.

4.1.1 Occurrence of the Vertical Slip

As the strike of fault trace changed from N60°E in the north to N24°W in the south (Table 1), the corresponding pattern of deformation in each area also changed from north

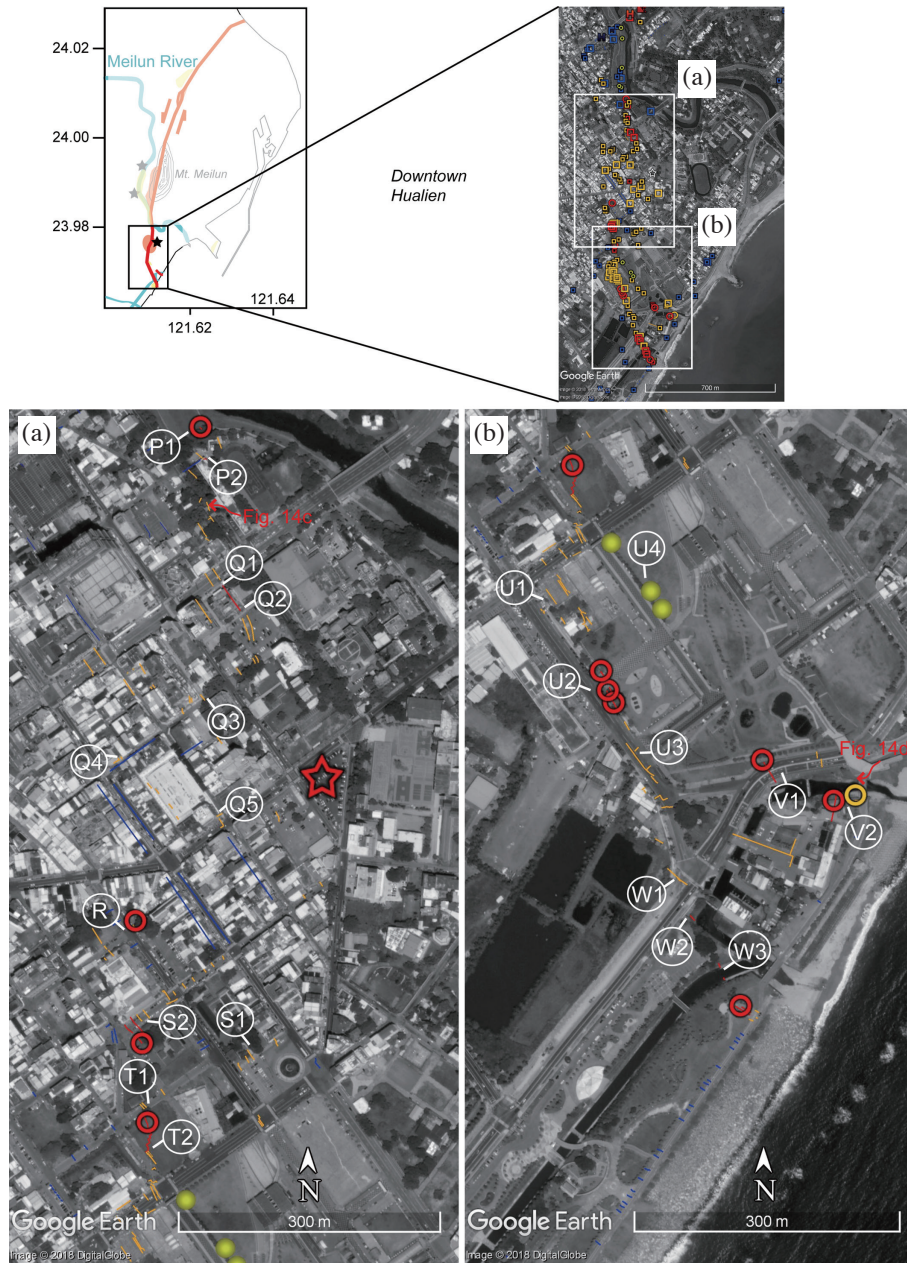


Fig. 8. Maps showing damage zones in downtown area. (a) Map showing the distribution of ruptures from sites P to T. In order to better visualize the fault trace, only rupture lines and points with surface rupture damage are plotted here. (b) Map showing the distribution of ruptures from sites U to W.

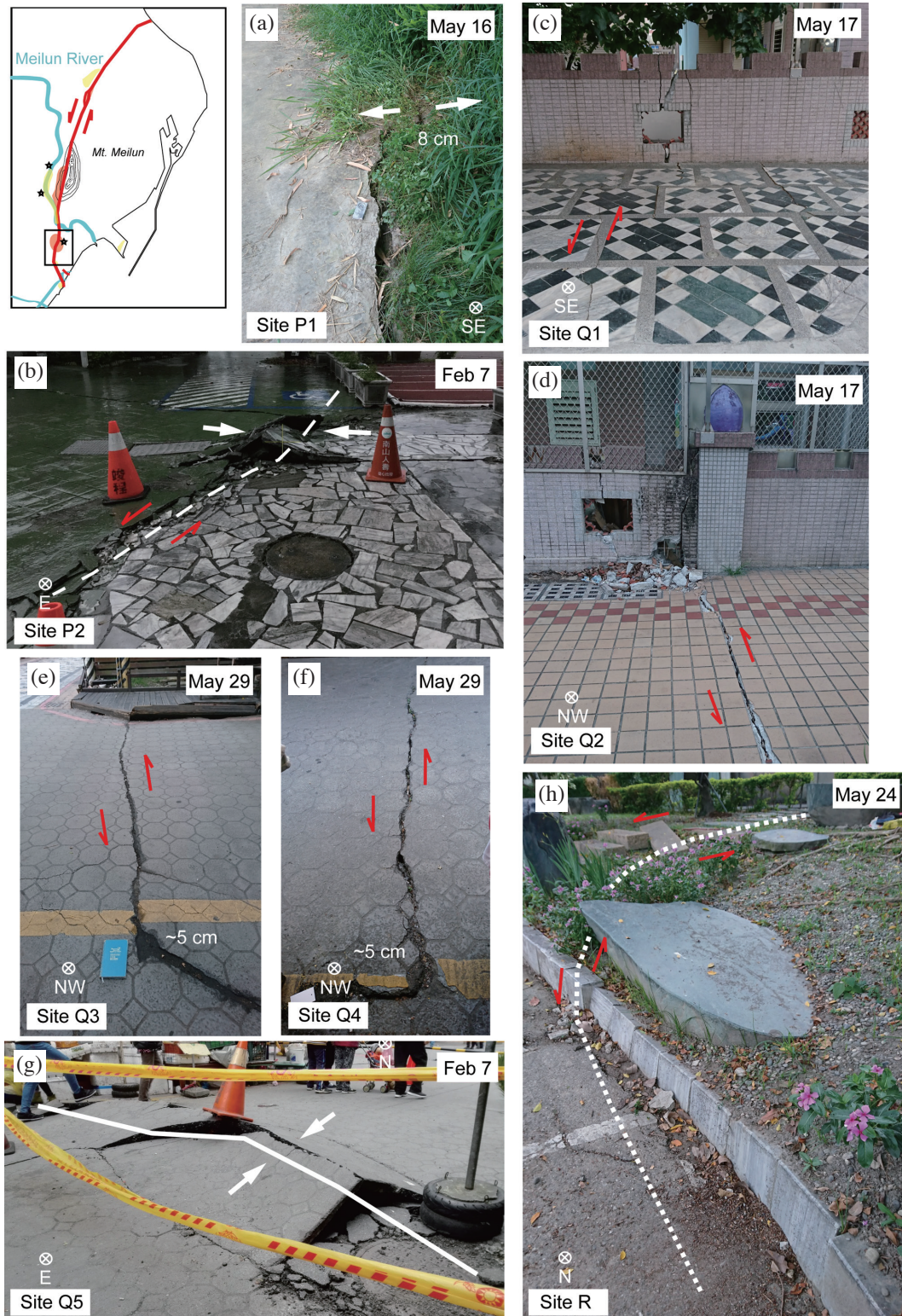


Fig. 9. Field photos of the representative ruptures. (a) Tensional cracks occurred north of the Mingli elementary school. (b) Push-up ridge and shears in the campus of Mingli elementary school. (c) Sinistral offset ran across the front door of the kindergarten. (d) Sinistral offset ran out from the back door of the kindergarten. (e) Sinistral offset of ca. 5 cm occurred at site Q3. (f) Sinistral offset of ca. 5 cm occurred at site Q4. (g) Push-up ridge occurred at site Q5. (h) Sinistral rupture offset the stone plate and the pavement bricks.

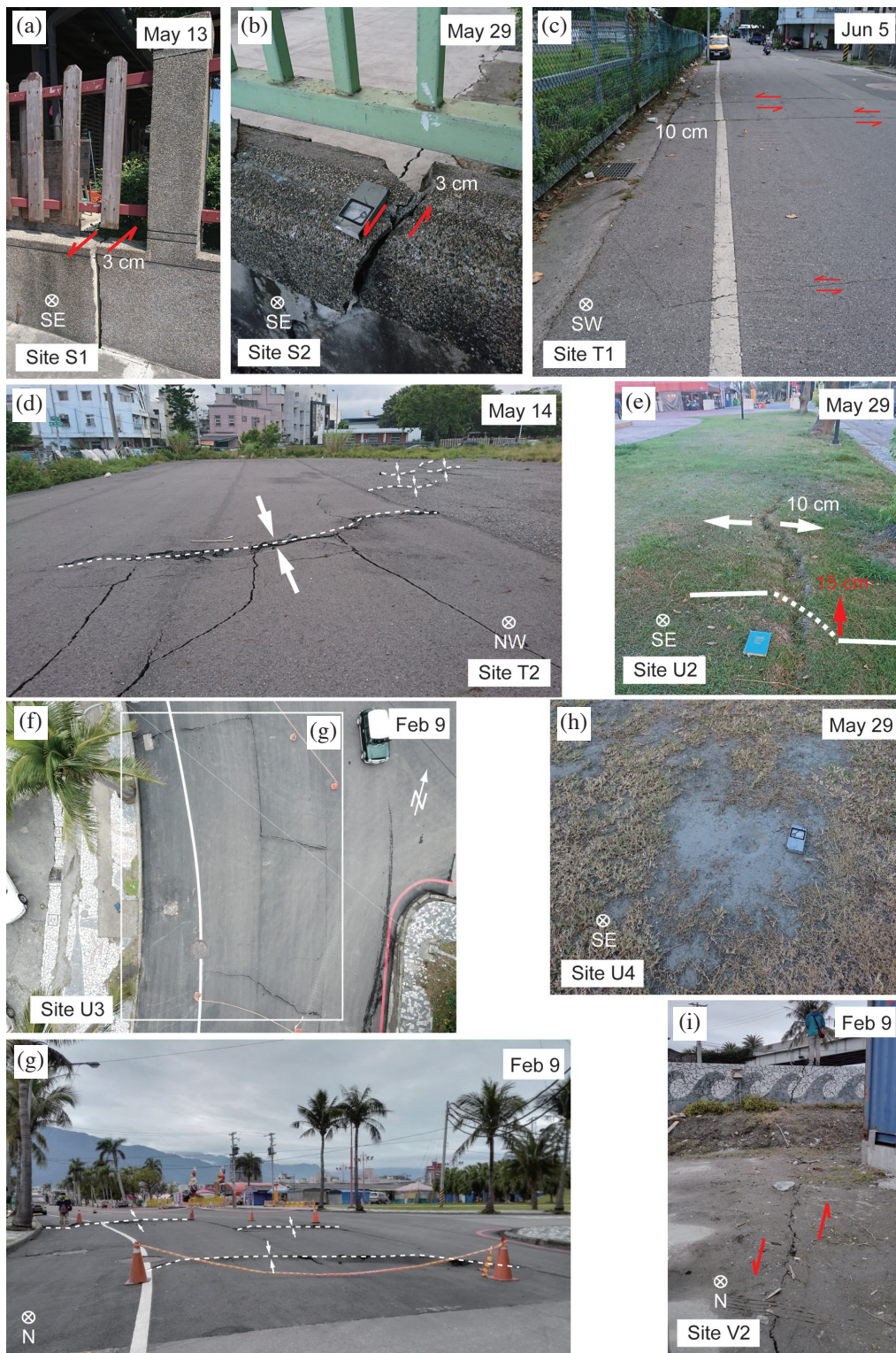


Fig. 10. Field photos of the representative ruptures. (a) The guardrail of the Hualien Railway Culture Park Hall 2 was offset about 3 cm. (b) The guardrail of the Hualien Railway Culture Park Hall 1 was offset about 3 cm. (c) The road mark was offset about 10 cm in total. (d) A series of push-up moletracks connected the northwest-striking shears. (e) Surface cracks aside the night market. (f) Drone image of the push-up ridges in front of the night market. (g) Close-up of push-up ridges at site U3. (h) Sand boils on the ground showing the features of liquefaction. (i) Sinistral ruptures ran across the stone wall and the ground surface in the yard of the Funeral Parlour.

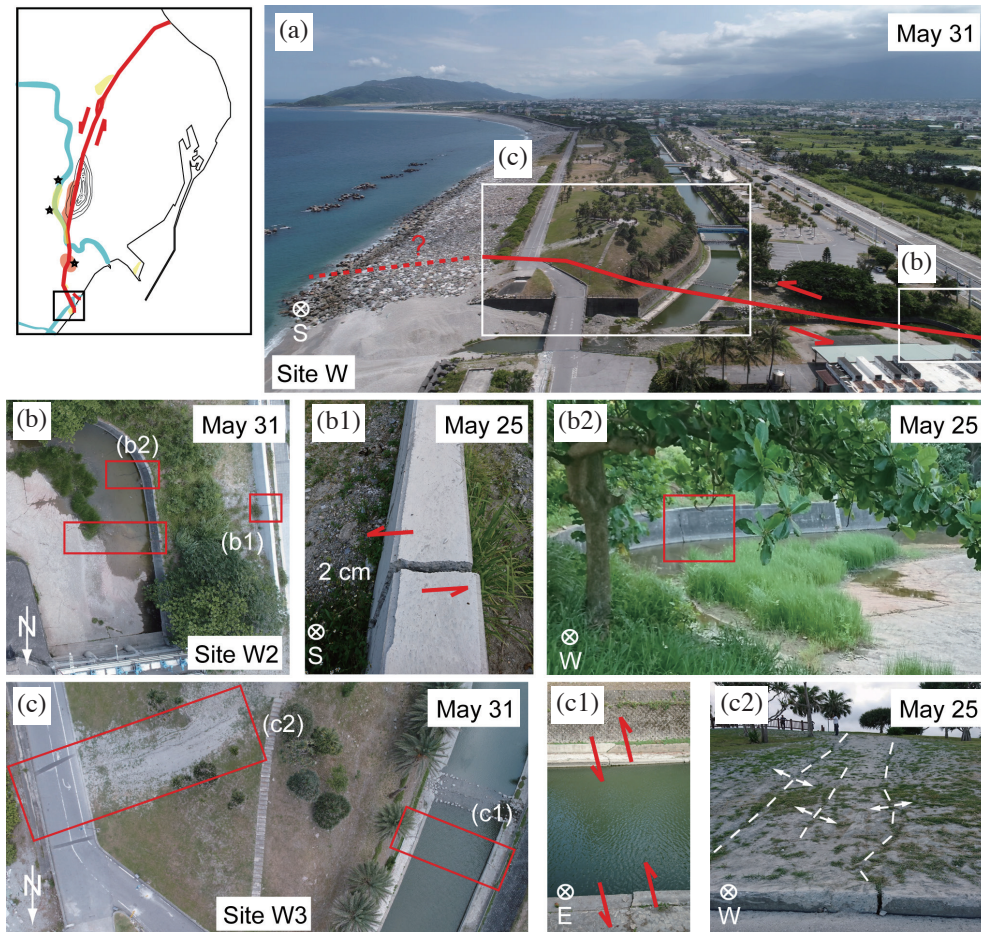


Fig. 11. Field photos of the representative ruptures. (a) Drone image showing the relative location of the south end. (b) The rupture passed through the Water Pumping Station from west to east. (b1) Rupture extended from north broke through the concrete wall. (b2) The wall of the revetment were damaged with tensional cracks. (c) Drone image showing the extension of the ruptures. (c1) The rupture passed through the channel from west to east. (c2) Prolonged en-echelon cracks occurred on the hillslope.

Table 1. Distribution and characteristics of the damage zones.

Segments		Sites	Strike	Horizontal offset (cm)		Vertical offset (cm)	Width of MDZ (m)		Width of SDZ (km)	
				Max.	Cum.	Max.	Max.	Avg.	Max.	Avg.
Chihsingtan Beach		A	N60°E	30.0	40.0	20.0	20	20	0.02	0.02
		B		30.0	30.0	0.0	22	22	0.1	0.1
		C		77.0	77.0	40.0	10	10	0.06	0.06
		D		-	-	-	10	10	0.05	0.05
		E		70.0	70.0	0.0	1	1	0.022	0.022
		F		70.0	70.0	0.0	20	20	0.037	0.03
	Avg.	N60°E	55.4	57.4	12.0					
North Meilun	North	G	N37°E	23.0	70.0	50.0	30	30	1	0.3
		H		20.0	20.0	30.0	10	10	0.1	0.1
		I		6.0	18.0	5.0	20	20	1	0.1
	South	J	N24°E	15.0	22.0	0.0	80	50	0.12	0.06
		K		30.0	30.0	0.0	10	10	0.03	0.03
		L		30.0	30.0	0.0	50	10	0.05	0.05
	Avg.	N31°E	20.7	31.7	14.2					
Mt. Meilun		M	N10°E	15.0	15.0	10.0	250	200	2.6	2.2
		N		5.0	5.0	8.0	250	200	2.6	2.2
		O		-	-	-10*	-	-	-	-
	Avg.	N10°E	10.0	10.0	9.0					
Downtown	North	P	N4°E	20.0	20.0	0.0	20	20	3.5	2.3
		Q		5.0	15.0	0.0	270	250	3.6	3.4
		R		3.0	9.0	0.0	270	250	3.4	3.4
		S		5.0	18.0	0.0	200	200	3.5	3.4
		T		4.0	10.0	0.0	100	100	4	4
	South	U	N24°W	16.0	16.0	15.0	100	100	3.8	3.4
		V		20.0	20.0	6.0	230	200	2.5	2.5
		W		5.0	10.0	0.0	230	200	2.8	2.5
Avg.	N5°W	9.8	14.8	2.6						

Note: * The negative value on site O represents subsidence associated with the riverine slumping and is not counted in the calculation of the average.

to south. In the northernmost Chihsingtan Beach, fault scarp was observed on the beach as the east side uplifted. In addition, arrays of Riedel shears, push-up ridges, and tensional cracks occurred at site B, forming a series of en-echelon folds (Figs. 12a1 to a4). The occurrence of fault scarp and folding indicates the component of vertical slip at this region. In fact, the vertical displacement is mostly observed in the north segments and soon decreases to almost undetectable south of site H.

4.1.2 The Development of Step-Overs and Restraining Bends

South of Chihsingtan Beach, most of the ruptures developed as en-echelon arranged synthetic Riedel shears with tensional components and were connected by synthetic push-up moletracks or ridges. Antithetic Riedel shears occurred sometimes with comparable or smaller amount of dextral offsets that accommodated the moving sense of deformed blocks. The bifurcated segments at sites J1 and J2 showed two typical geometry of surface ruptures associated with the Milun Fault (Fig. 12b1): at J1 (Fig. 12b3), the fault ruptured as offset, separation, or partially overlapped segments with NS-striking sinistral or northwest-striking dextral shears (description of step-over geometry follows; Barka and Kadinsky-Cade 1988; Mitra and Paul 2011; Fig. 2c). At J2 (Fig. 12b2), northwest-striking Riedel shears of right- or left-lateral sense both occurred. Hard links between the segments developed as the northeast-striking push-up moletracks, forming gentle and sharp restraining bends. Down to the south, site T (Fig. 12c1) provided another example showing a series of synthetic Riedel shears propagated southward and the restraining bends consequently developed (Fig. 12c2).

4.1.3 Step-Overs in Downtown Hualien

In downtown Hualien, an array of northwest-striking ruptures formed a prominent linking damage zone with right stepping step-overs fully or partially overlapped with each other and accompanied by some minor northeast-striking push-up ridges (Figs. 12d1 and d2). The ruptures did not evolve into through-going lineaments and hence resulted in relative wider restraining areas between the step-overs (Wakabayashi et al. 2004; Cunningham and Mann 2007). Field observation of continuous damage along the pavements, arcades, and floors of houses demonstrated the existence of transpression zones. However, as the separation zone between the fault tips is relative small, an alternative explanation of these widely-spread shears is that these deformation may correspond to an earlier stage of rupture propagation within the downtown where the surface is densely covered by the concrete and steel buildings (Riedel 1929; Davis et al. 2000, 2011). Nevertheless, as the buildings and

infrastructures take up the densely populated downtown area and hinder our recognition of the displacement caused by the interactions between the step-overs, the value of the on-fault displacement may therefore be underestimated.

4.2 Slip Distribution of the Milun Fault and Its Implications

4.2.1 Distributed Slip Along and Across the Fault

The orientation, amount of offsets, and the width of damaged areas across the fault trace all appeared to vary from north to south (Fig. 13, relevant records are listed in Table 1). The strike of the fault evolved counter-clockwise from northeast to northwest and formed a curved trace concave to the east. The maximum vertical displacement was measured as 50 cm on the north segments (site G) and the amount of vertical offset decreased to almost undetectable toward south. Horizontal displacement showed a similar trend with a maximum sinistral offset of 77 cm occurred in the north end of the fault (site C) and the averaged sinistral offsets decreased from 57 cm in the north to 15 cm in the south.

According to the category of investigated damage points, we have estimated the width of MDZ and SDZ. The width of MDZ represents how far the slip of a fault can be accommodated and the width of SDZ represents how far the impact of ground motion can persist from the fault core area. The width of MDZ was mostly very limited within the range of 1 - 20 m along the wall damage zones on the northern part of the fault except for site J (up to 80 m) where bifurcated segments occurred, developing prominent step-overs and restraining bends. In areas of the linking damage zones, the width of MDZ increased as the slip appeared to be distributed across a much wider area along the discontinued segments. In downtown Hualien the width can even reach 270 m wide, denoting the broad range of the damage zone. Similarly to MDZ, the width of the SDZ significantly increased from tens of meters in the north to 2 - 4 km in the central to south part of the fault.

In general, the amount of offset decreases toward south while the width of damage zone increases. The vertical displacement is larger in the north and becomes insignificant in the south part of the fault. Similarly, the sinistral displacement is large and localized in the north and decreases to the south with a broad range of distributed slip.

4.2.2 The Discrepancy Between On-Site Measurements and Remote Sensing Estimates

The coseismic offset estimated by satellite images, continuous and campaigned GPS all suggested the horizontal and vertical displacement to be over 50 cm (CGS 2018; Yang et al. 2018; Yen et al. 2018), which is in fact significantly higher than most of the on-site measurements. In the north segments, the observed max. 50-cm-vertical

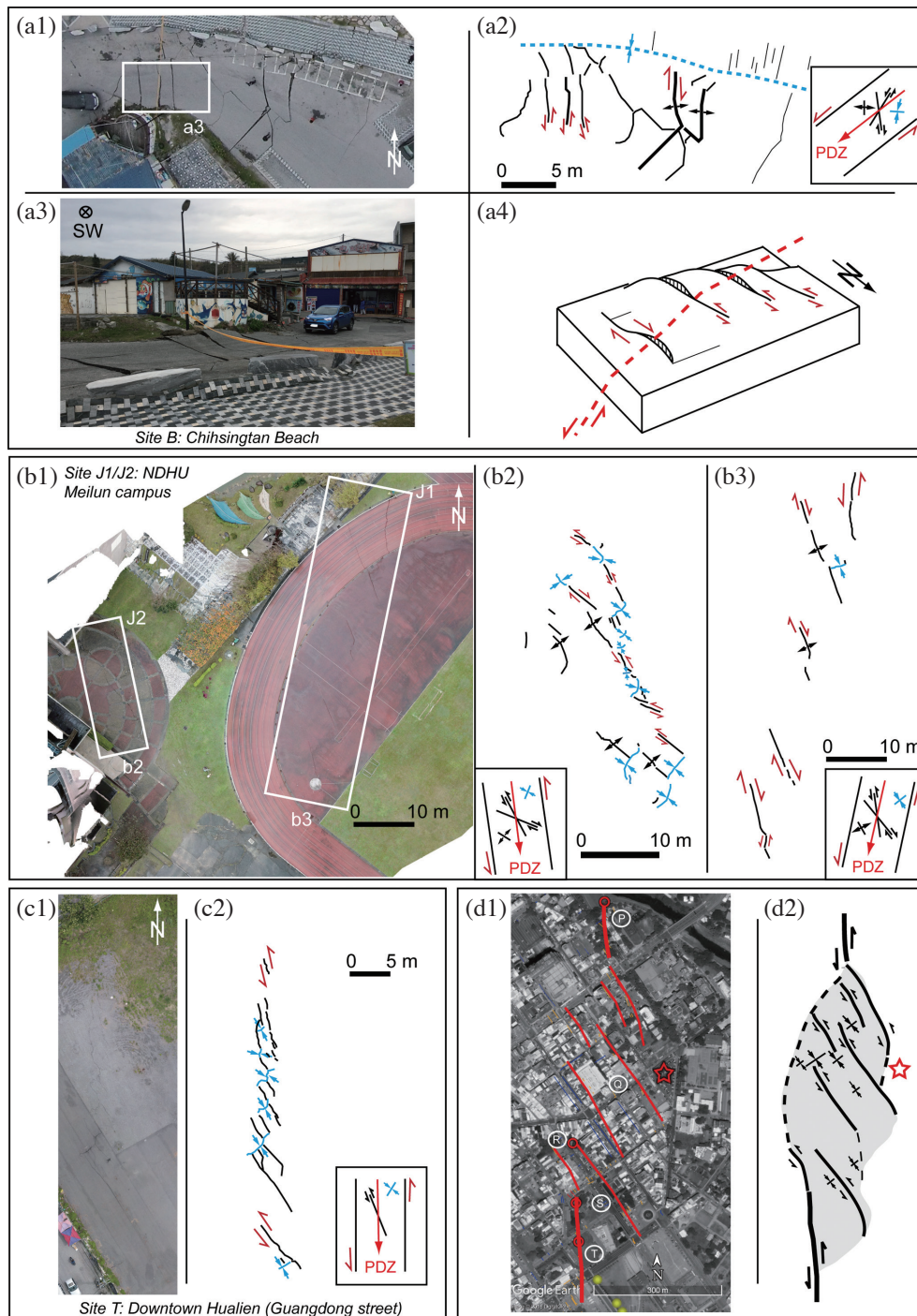


Fig. 12. Photos and illustrations showing the representative structures occurred along the rupture zones. (a1) Drone image of the Chihsingtan Parking Lot. (a2) Schematic illustration of the associated ruptures. Inset shows the conceptual setting of the stress field. (a3) Field photo of the surface deformation. (a4) Schematic diagram of the en-echelon folding. (b1) Drone image of the Meilun campus, NDHU. (b2) Schematic illustration of the rupture lines in front of the gym. (b3) Schematic illustration of the rupture lines in the track field. (c1) Drone image of the Guangdong Street field at site T. (c2) Schematic illustration of the rupture lines in the field. (d1) Close-up of the major ruptures in downtown area from sites P to T. (d2) Schematic illustration of the rupture lines showing the arrangement of right stepping step-overs and a wide zone of transpression across the downtown.

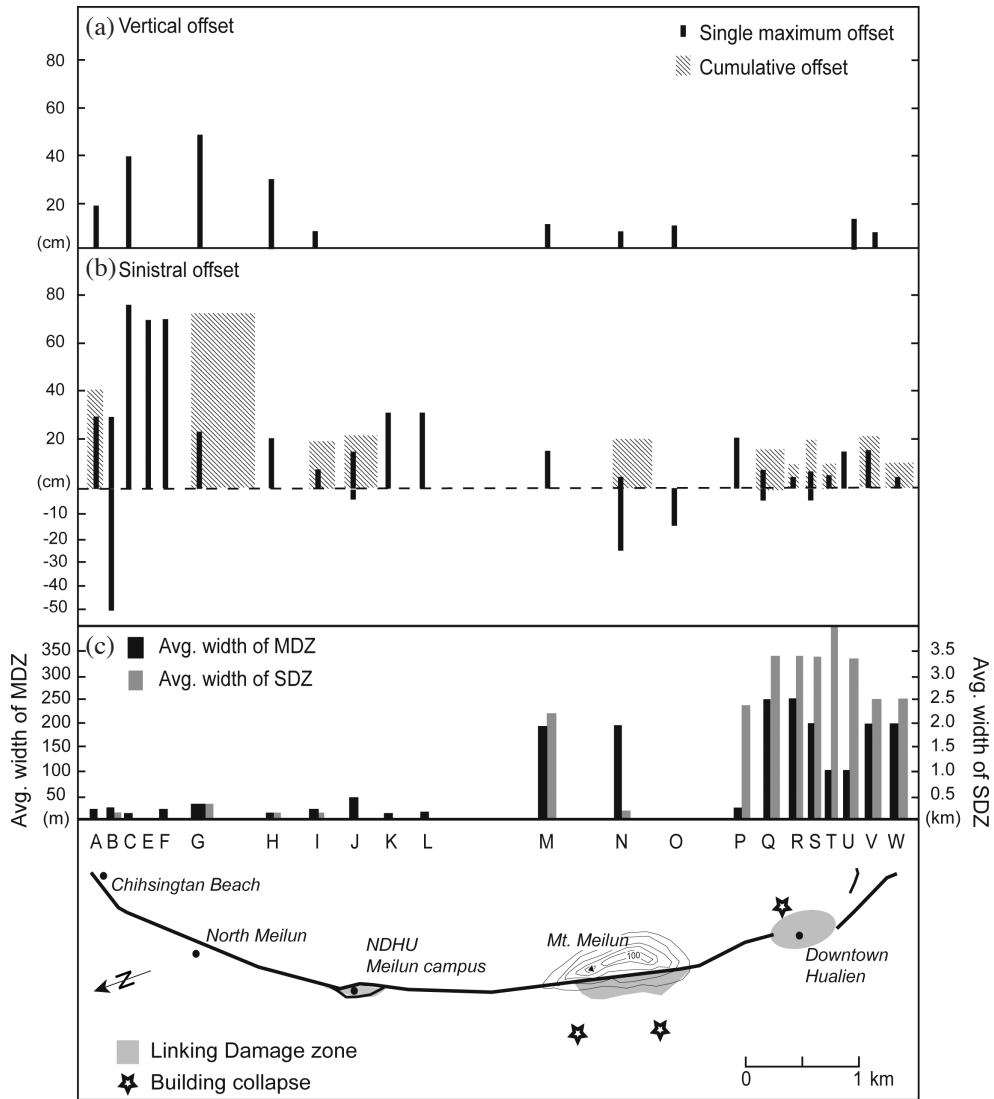


Fig. 13. The distribution and characteristics of offsets along the fault. (a) The vertical offset along the fault. (b) The sinistral offset along the fault. Note that dextral offsets are drawn as negative values. Cumulative offsets are presented as areas of slant lines in sites with distributed offsets. (c) The average width of MDZ and SDZ across the fault.

and 70-cm-sinistral offsets are comparable with the remote sensing estimates. As the fault extended toward south, the surface displacement measured on the outcrops apparently do not match the observations of remote sensing. Yen et al. (2018) have concluded that much of the Meilun tableland uplifted several tens of centimeters (up to 45 cm) and moved northeast ca. 50 cm during the 2018 earthquake according to their InSAR, GPS, and 3D displacement model. However, the average sinistral offsets from the on-site measurements on the central-south part of the fault only count 10 - 15 cm.

In areas with step-overs, the slip may be distributed and resulted in ruptures with varied displacements across the damage zone. As Kim and Sanderson (2005) proposed, the estimated displacement near the linkage zone can be quite different depending on the evolutionary stages of the separate segments. For instance, displacement can be almost zero at the early stage when the fault tips just start to interact. As more hard linked segments occur, greater displacement can accumulate around the linkage zone as the two segments start to act as one through-going fault. In the linking damage zone of downtown Hualien, most of the step-overs are not connected, thus the displacement may not be able to accumulate and therefore lead to an underestimate.

To reduce the limitation of single on-fault measurements, in areas with overstepping segments we attempted to estimate the cumulative offset by including the associated tension, shortening from the push-up structures as Angelier et al. (2004) suggested. It is to note that the direct measurement of an offset from a rupture is already an underestimate of true slip, let alone to further calculate the cumulative offsets from the amount of associated tension and compression. The cumulative offsets reported here hence only offer the minimum estimate of true slip. In addition, as discussed earlier, the artificial constructions above the linking damage zone may hamper our understanding on the distribution of slip. That being said, even if we consider the cumulative offsets to be the lowest limit of the true slip, the measurements are still significantly smaller than the GPS estimates. The discrepancy is evident and coincides with the surface deformation detected by GPS and InSAR techniques (CGS 2018; Yang et al. 2018; Yen et al. 2018), revealing the rotation movement of the upthrown block. The 3D surface displacement mode of Yen et al. (2018) shows that the displacement increases to the east and the northeast across the uplifted terrace rather than being localized along the fault trace. This discrepancy between the on-site measurements and the geodetic observations therefore suggests that the surface deformation not only distributed from north to south but also varied perpendicular to the strike of the fault.

4.2.3 The Seismotectonic Implications

The occurrence and distribution of step-overs are usually controlled by the rheological properties of the material,

pre-existing structures, steps of rupture planes in the subsurface, and the change of stress field (Westaway 1995; Wakabayashi et al. 2004; Chemenda et al. 2016). The pattern of distributed deformation indicates that the near surface deformation in fact accommodated the internal strains rather than showing relative offsets between individual ruptures. According to the high resolution optical image correlation of stereo Pleiades images, Kuo et al. (2018) argued that ~60% of the deformation may have occurred as off-fault deformation within a shallow zone of the uppermost crust where the Holocene alluvial sediments may provide the weak contrast of material strength.

In addition to the properties of the underlying strata, the intricate underground architectures may also play an important role. Yen et al. (2018) proposed that the distribution of the displacement is the result of forced slip on curved horse-tail splays in a zone of complex wrench tectonics. However, the relationship between the Milun Fault and the structure at depth remains uncertain. Chen et al. (2014) argued that this area is the southern tip of the extruded northeast Taiwan and displayed its own behaviour of block rotation. Shyu et al. (2016a), on the other hand, proposed that the Milun Fault is one of the branch faults associated with the detachment underneath the sediments of Longitudinal Valley. Further investigations targeting the near surface profiling such as shallow seismic reflection and electrical resistivity survey should enable more insights of the subsurface configurations.

4.3 Repeated Ruptures of the Milun Fault

Although the coseismic rupture of the 1951 earthquake has been mapped according to the photographs and reports from the newspapers and the Central Weather Bureau, the exact location of the offsets and the extension of the fault segments were ambiguous, especially in the downtown area (Cheng et al. 1999; CGS 2010). The ruptures of the 2018 earthquake delineated in section 3 provided the opportunity to compare the coseismic surface ruptures and revisit the extension of the Milun Fault. As most of the 1951 photos showed the damage of houses, there are only a few of them displaying validated surface ruptures with the information of named locality. The comparisons between the 1951 photos and the on-site observation of the 2018 ruptures hence are of significant importance to show whether the Milun Fault has generated repeated ruptures in the damage zones.

4.3.1 Earlier Events at Chihsingtan

At the Chihsingtan area, an excavation near the damaged house was operated to repair the floor of the house (near site C2, excavation location is labelled in Figs. 3a and 4e) and hence revealed the earlier events of offset (Figs. 14a1 and a2). Five major strata and two faults were identified below the concrete floor and the backfill

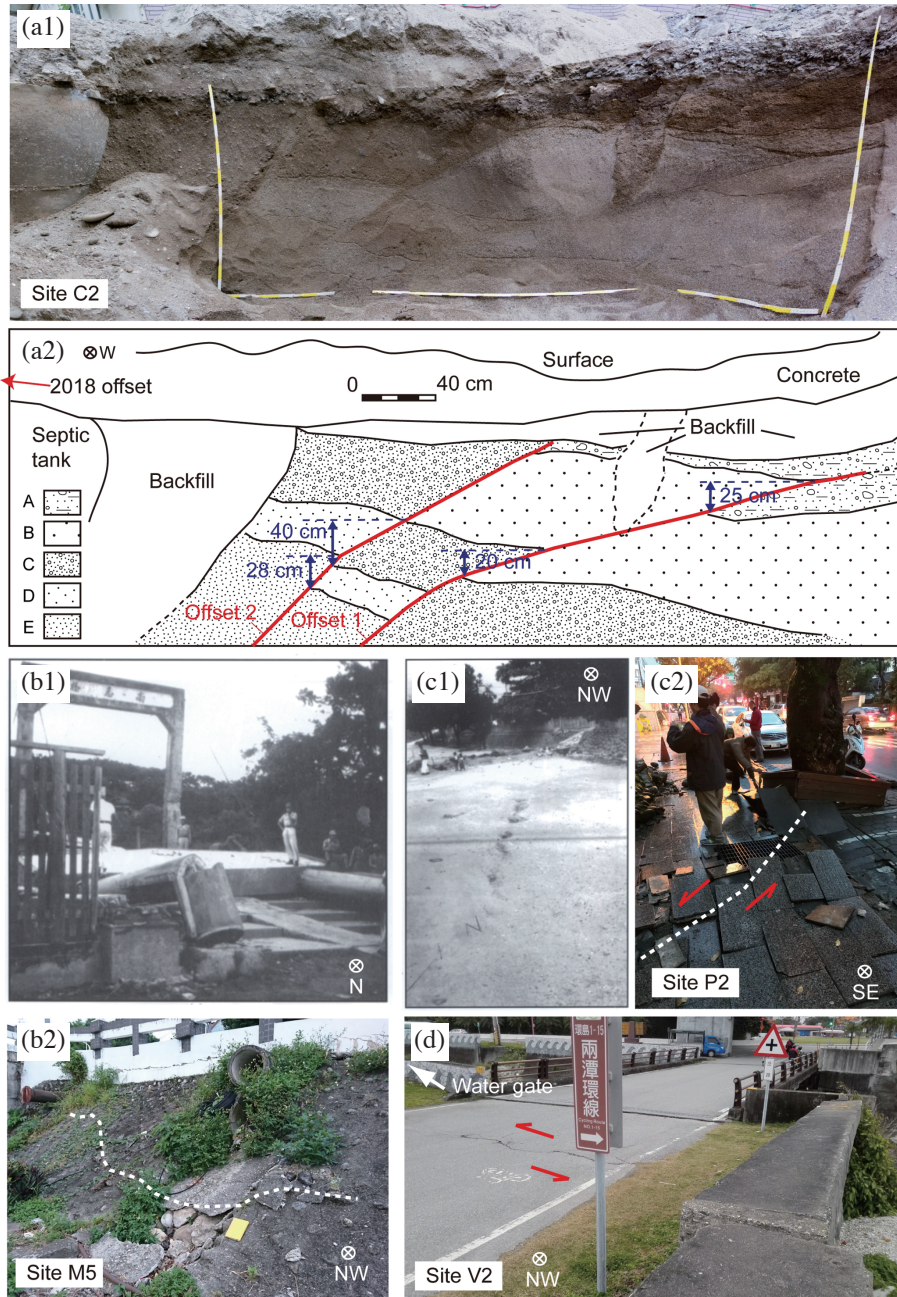


Fig.14. (a1) The photo of the excavation beside the damaged house at the Chihsingtan Area. (a2) Schematic illustration of the offset strata. (b1) Historic photo showing the damage at the north end of Shangzhi Bridge. (b2) Damaged revetment below the north end of Shangzhi Bridge. (c1) The northwest-striking cracks occurred on the road by the elementary school. (c2) Disrupted tiles by the elementary school. (d) Sinistral offsets near the Nanbin Water Gate.

layers. The uppermost unit A is composed of brown coarse sand and very fine gravel with some lamination. Below that, the unit B comprises massive white sand to coarse sand with coarsening upward grading. The underlying unit C is poorly sorted, comprising yellow to brown fine sand to sand with occasional occurrence of pebble size clasts. Unit D is composed of white coarse sand with fining upward grading. The lowermost unit E comprises well-sorted yellow sand and occurs as a massive unit. The two offset planes cut through the five units and display vertical offsets of 20 - 40 cm. The offset 1 displays a vertical displacement of 25 cm between A and B units, and 20 cm between B and C units; the offset 2 displays a vertical displacement of 40 cm between C and D units, and 28 cm between D and E units.

Both of the offsets did not reach the surface nor the backfill, indicating that these vertical displacements occurred prior to the 2018 earthquake. In addition, the back-filled V shaped burrow penetrated unit C and even cut across the plane of offset 1, suggesting that the digging of the burrow post-dated the offset. The two offsets did not rupture during the 2018 earthquake and the coseismic rupture of the 2018 earthquake occurred at the rear corner of the house, recording an uplift of ~27 cm as mentioned in section 3.1. The two offset planes in the excavation may either represent two individual events or a synchronous movement with two rupture segments. The apparent cut-through relationships of the preserved stratigraphy cannot distinguish the two scenarios and therefore suggest at least one earlier event in this location. Although offsets of the 1951 earthquake have been previously reported in the Chihshintan area, there was no exact information about where the damaged house and offsets really located. The stratigraphic profile from this excavation site clearly demonstrates the records of repeated ruptures in the Chihshintan area. The offset pattern inside the excavation is consistent with the 2018 earthquake, showing the east side of the fault to be the upthrown block and the occurrence of these vertical displacements validates the contribution of the Milun Fault upon the formation of local topography for the north Hualien.

4.3.2 Positions of Likely Repeated Ruptures

South of Mt. Meilun, the rupture passed through the north end of the Shangzhi Bridge and caused damage on the pavements and revetments where similar damage has been reported in 1951 (south of site M5). In 1951, the north end of the Shangzhi Bridge was severely damaged as ground cracks formed (Cheng et al. 1999) and the monumental archway collapsed (Fig. 14b1). The coseismic offset of the 2018 earthquake ruptured through the embankment and disrupted the water pipes (Fig. 14b2). The bridge was closed for days to be repaired and reinforced after the 2018 earthquake.

South of the Meilun River, the fault ruptured around the campus of Mingli elementary school (site P2) where evi-

dent surface ruptures were reported in 1951 as well. According to the report (Cheng et al. 1999), the 1951 earthquake produced en-echelon tensional cracks along the road by the elementary school (Fig. 14c1). After the 2018 earthquake, significant ruptures with sinistral slip also occurred and disrupted the paved tiles (Fig. 14c2). Although we do not have the exact coordinates of the 1951 ruptures, the orientation of the tensional cracks (N10°W on the road and N40°W inside the school; Cheng et al. 1999) are consistent with the 2018 earthquake (N20 - 50°W).

In 1951, newspapers and reports have documented that the south end of the fault passed through the Nanbin Water Gate, causing the embankment to collapse, and terminated its on-land rupture (Cheng et al. 1999). The embankment is now dismantled and hence the location of the Water Gate became ambiguous. There are two possible candidates for the location of the damaged Water Gate in 1951: the Water Pumping Station near Nanbin Park (site W) and to the east a lock gate currently called Nanbin Water Gate (site V). Judging from the relative position to the adjacent coastal line, site V may more likely be the one that has experienced repeated ruptures (Fig. 14d).

4.3.3 The Ruptures in Downtown Hualien

Most of the previous researches illustrated the Milun Fault as the western boundary along the tableland topography (the uplifted late Quaternary marine terrace) on the north and central sections of the fault (Lin and Hsiao 1998; Yamaguchi and Ota 2004; CGS 2010; Shyu et al. 2016b). However, to the south of the Mt. Milun, the identification of the fault became ambiguous because the topography is relatively flat and the records of the 1951 earthquake are in lack of credible coordinates. The 1951 ruptures in downtown Hualien were compiled as three branch faults splaying from the south of the Mt. Milun, crossing the city, and reconnected before the fault extended towards the Pacific (Hsu 1962; CGS 2010).

Similarly, the ruptures of the 2018 were arranged as overlapping step-overs in the downtown region, forming a linking damage zone with several subsidiary traces in a wide transpressional area. Figure 15 shows that between sites P and T, most of the 2018 damage points located within the damage zone defined by the 1951 earthquake but not necessarily on the three branches. We argue that the previously mapped fault segments may not really reflect the location of the 1951 surface ruptures because the outcrops were obscured. However, the extension of the three branches presented a first order enveloping range of the damage area. The 2018 surface ruptures provide a refined surface mapping with a much higher resolution in this aspect and suggest that the damage assessment in downtown Hualien should emphasize more on segmented faults with distributed slip than a single through-going fault.

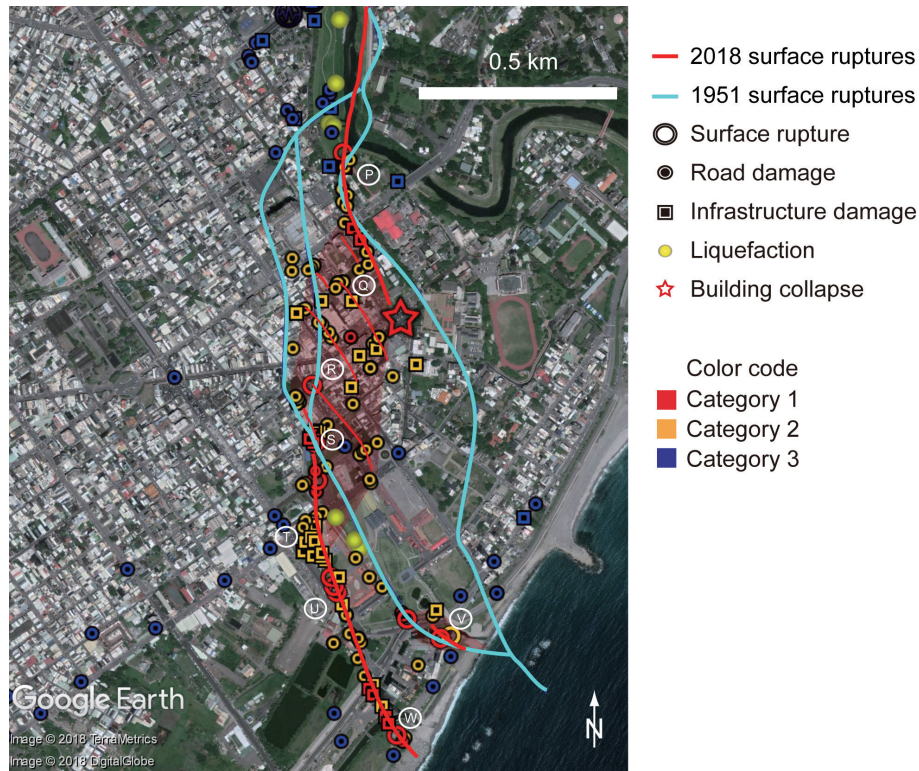


Fig. 15. The fault traces of the 1951 and the 2018 earthquakes.

4.4 Inspirations for Future Assessments of Seismic Hazards

After the February 6 earthquake, enormous efforts have been put into the field investigation, GPS networking, radar image analyses, and UAV photographing. Rupture identification on high resolution drone images greatly helped the detailed mapping of the fault trace, but still missed some outcrops that disappeared due to the urgent repairs proceeded right away after the shock. A more organized and efficient collaboration between the surface survey and UAV photographing teams is highly recommended in future hazard investigation to facilitate the overall picture of damaged areas.

Comparisons with the 1951 records prove that the Milun Fault is capable of producing repeated ruptures in the damage zones. The amount of offsets in each segment and the exact location of ruptures are hence of significant importance. In general, although there are uncertainties in the previous documents of the 1951 earthquake, the 2018 earthquake generated very similar patterns of surface ruptures along the Milun Fault. This allows us to map the distribution of surface ruptures in a higher resolution with exact coordinates and base on that a more reliable model of seismic risk assessment can be established in the future. To conclude, the rupture features differ notably with respect to different segments. The development of step-overs and the extension of damage zones may be controlled by the complex under-

ground structures. It is still not clear whether there are steps of fault planes, whether the detachment developed beneath the sediments, and how the surficial ruptures connected, merged, or offset in the subsurface. Future attempts to clarify the subsurface structures will be crucial to estimate upcoming seismic hazards.

5. CONCLUSION

The 2018 Hualien earthquake evoked public awareness on the seismic risks of the Milun Fault. As the northernmost segment of the Longitudinal Valley Fault, the Milun Fault displayed a variety of surface deformation showing a combination of left-lateral strike and vertical slip. Extensive field survey and investigations on drone images after this earthquake provided robust datasets documenting the distribution, magnitude, types, and damaged areas of the surface rupture zones along the 7.5-km-long fault trace and revealed a distributed pattern of segmented slip. The ruptures occurred as arrays of Riedel shears and formed right-stepping step-overs and restraining bends in the linking damage zones. Both of the vertical and horizontal slip decreased towards south and became more distributed. From the hazard assessment point of view, it is vital to gain the knowledge of the segmented slip, the deformation forms of PDZ, and the distribution of damage zones to mitigate future loss from repeated seismic events. We expect the data presented here

to offer a solid base for the development of the regional tectonic models and further seismic risk assessment.

Acknowledgements We thank the groups of ETEC and Dong Hwa University for the support of extensive field investigations. We are also grateful for the intense and valuable discussions with Dr. Yu-Ting Kuo and Yu Wang. The comments and suggestions from the anonymous reviewers greatly helped us to improve this manuscript.

REFERENCES

- Angelier, J., F. Bergerat, M. Bellou, and C. Homberg, 2004: Co-seismic strike-slip fault displacement determined from push-up structures: The Selsund Fault case, South Iceland. *J. Struct. Geol.*, **26**, 709-724, doi: 10.1016/j.jsg.2003.07.006. [Link]
- Aviles, C. A., C. H. Scholz, and J. Boatwright, 1987: Fractal analysis applied to characteristic segments of the San Andreas Fault. *J. Geophys. Res.*, **92**, 331-344, doi: 10.1029/JB092iB01p00331. [Link]
- Barka, A. A. and K. Kadinsky-Cade, 1988: Strike-slip fault geometry in Turkey and its influence on earthquake activity. *Tectonics*, **7**, 663-684, doi: 10.1029/TC007i003p00663. [Link]
- Barrier, E. and J. Angelier, 1986: Active collision in eastern Taiwan: The Coastal Range. *Tectonophysics*, **125**, 39-72, doi: 10.1016/0040-1951(86)90006-5. [Link]
- Bonilla, M. G., 1975: A review of recently active faults in Taiwan. U.S. Geological Survey Open-File Report 75-41, Version 1.1, Reston, VA, 42 pp. Available at <http://geopubs.wr.usgs.gov/open-file/of75-41/>.
- Bonilla, M. G., 1977: Summary of Quaternary faulting and elevation changes in Taiwan. *Mem. Geol. Soc. China*, **2**, 43-55.
- CGS, 2010: Active Fault Map of Taiwan, Central Geological Survey, Taipei. Available at http://fault.moeacgs.gov.tw/TaiwanFaults_2017/images/PDF/20180206report.pdf.
- CGS, 2018: Geological Report of 2018 Hualien Earthquake, Central Geological Survey Report, Taipei, 131 pp. (in Chinese)
- Chemenda, A. I., O. Cavalié, M. Vergnolle, S. Bouissou, and B. Delouis, 2016: Numerical model of formation of a 3-D strike-slip fault system. *C. R. Geosci.*, **348**, 61-69, doi: 10.1016/j.crte.2015.09.008. [Link]
- Chen, C.-Y., J.-C. Lee, Y.-G. Chen, and R.-F. Chen, 2014: Campaigned GPS on Present-day crustal deformation in northernmost Longitudinal Valley preliminary results, Hualien Taiwan. *Terr. Atmos. Ocean. Sci.*, **25**, 337-357, doi: 10.3319/TAO.2013.12.25.01(TT). [Link]
- Cheng, S.-N., Y. T. Yeh, M.-T. Hsu, and T.-C. Shin, 1999: Photo Album of Ten Disastrous Earthquakes in Taiwan, Central Weather Bureau, 290 pp.
- Choi, J.-H., P. Edwards, K. Ko, and Y.-S. Kim, 2016: Definition and classification of fault damage zones: A review and a new methodological approach. *Earth-Sci. Rev.*, **152**, 70-87, doi: 10.1016/j.earscirev.2015.11.006. [Link]
- Chu, H.-T. and M.-S. Yu, 1997: The Relationships between Earthquakes and Faults in the Taitung Longitudinal Valley, National Science Council Project Report, Project No. NSC-86-2116-M-047-002, Taipei, 133 pp. (in Chinese)
- Cunningham, W. D. and P. Mann, 2007: Tectonics of strike-slip restraining and releasing bends. *Geol. Soc. Lond. Spec. Publ.*, **290**, 1-12, doi: 10.1144/sp290.1. [Link]
- CWB, 2018: Seismicity Report of No. 22 Earthquake, Central Weather Bureau, Taipei. Available at <https://www.cwb.gov.tw/V7e/earthquake/seismic.htm>.
- Davis, G. H., A. P. Bump, P. E. García, and S. G. Ahlgren, 2000: Conjugate Riedel deformation band shear zones. *J. Struct. Geol.*, **22**, 169-190, doi: 10.1016/S0191-8141(99)00140-6. [Link]
- Davis, G. H., S. J. Reynolds, and C. F. Kluth, 2011: Structural Geology of Rocks and Regions, 3rd Edition, John Wiley & Sons, 864 pp.
- Hsu, T. L., 1962: Recent faulting in the Longitudinal Valley of eastern Taiwan. *Mem. Geol. Soc. China*, **1**, 95-102.
- Hsu, Y.-C., C.-P. Chang, H. Kuo-Chen, J.-Y. Yen, C.-C. Wang, B.-L. Wu, Y.-H. Chang, W.-Y. Chang, and C.-H. Lu, 2018: Investigating surface ruptures and co-seismic deformation of 0206 Hualien earthquake using field survey and remote sensing. *Sino-Geotechnics*, **156**, 15-24. (in Chinese)
- Kim, Y.-S. and D. J. Sanderson, 2005: The relationship between displacement and length of faults: A review. *Earth-Sci. Rev.*, **68**, 317-334, doi: 10.1016/j.earscirev.2004.06.003. [Link]
- Klinger, Y., 2010: Relation between continental strike-slip earthquake segmentation and thickness of the crust. *J. Geophys. Res.*, **115**, doi: 10.1029/2009JB006550. [Link]
- Kuo, Y.-T., Y. Wang, J. Hollingsworth, S.-Y. Huang, R. Y. Chuang, C.-H. Lu, Y.-C. Hsu, H. Tung, J.-Y. Yen, and C.-P. Chang, 2018: Shallow fault rupture of the Milun Fault in the 2018 Mw 6.4 Hualien Earthquake: A high-resolution approach from optical correlation of Pléiades satellite imagery. *Seismol. Res. Lett.*, **90**, 97-107, doi: 10.1785/0220180227. [Link]
- Kuo-Chen, H., Z.-K. Guan, W.-F. Sun, P.-Y. Jhong, and D. Brown, 2018: Aftershock sequence of the 2018 M_w 6.4 Hualien earthquake in eastern Taiwan from a dense seismic array data set. *Seismol. Res. Lett.*, **90**, 60-67, doi: 10.1785/0220180233. [Link]
- Lee, S.-J., T.-C. Lin, T.-Y. Liu, and T.-P. Wong, 2018: Fault-to-Fault Jumping Rupture of the 2018 Mw 6.4

- Hualien Earthquake in Eastern Taiwan. *Seismol. Res. Lett.*, **90**, 30-39, doi: 10.1785/0220180182. [[Link](#)]
- Lin, C.-W., W.-S. Chen, Y.-C. Liu, and P.-T. Chen, 2009: Active Faults of Eastern and Southern Taiwan, Central Geological Survey, Taiwan.
- Lin, M.-S. and C.-L. Hsiao, 1998: Strike-Slip Tectonics in the Milun Conglomerate Terrace. *Eastern Taiwan Studies*, **3**, 13-29, doi: 10.6275/JETS.3.13-29.1998. (in Chinese) [[Link](#)]
- Malavieille, J., S. E. Lallemand, S. Dominguez, A. Deschamps, C.-Y. Lu, C.-S. Liu, P. Schnuerle, J. Angelier, J. Y. Collot, B. Deffontaines, M. Fournier, S. K. Hsu, J. P. Le Formal, S. Y. Liu, J. C. Sibuet, N. Thureau, and F. Wang, 2002: Arc-continent collision in Taiwan: New marine observations and tectonic evolution. In: Byrne, T. B. and C.-S. Liu, *Geology and Geophysics of an Arc-Continent Collision, Taiwan*, Vol. 358, Geological Society of America, 187-211, doi: 10.1130/0-8137-2358-2.187. [[Link](#)]
- McClay, K. and M. Bonora, 2001: Analog models of restraining stepovers in strike-slip fault systems. *AAPG Bull.*, **85**, 233-260, doi: 10.1306/8626c7ad-173b-11d7-8645000102c1865d. [[Link](#)]
- Mitra, S. and D. Paul, 2011: Structural geometry and evolution of releasing and restraining bends: Insights from laser-scanned experimental models. *AAPG Bull.*, **95**, 1147-1180, doi: 10.1306/09271010060. [[Link](#)]
- Riedel, W., 1929: Zur Mechanik geologischer Brucherscheinungen ein Beitrag zum Problem der Fiederspatten. *Zentbl. Miner. Geol. Palaont. Abt.*, 354-368.
- Scholz, C. H., 1990: *The Mechanics of Earthquakes and Faulting*, Cambridge University Press, New York, 439 pp.
- Segall, P. and D. D. Pollard, 1980: Mechanics of discontinuous faults. *J. Geophys. Res.*, **85**, 4337-4350, doi: 10.1029/JB085iB08p04337. [[Link](#)]
- Shyu, J. B. H., L.-H. Chung, Y.-G. Chen, J.-C. Lee, and K. Sieh, 2007: Re-evaluation of the surface ruptures of the November 1951 earthquake series in eastern Taiwan, and its neotectonic implications. *J. Asian Earth Sci.*, **31**, 317-331, doi: 10.1016/j.jseae.2006.07.018. [[Link](#)]
- Shyu, J. B. H., C.-F. Chen, and Y.-M. Wu, 2016a: Seismotectonic characteristics of the northernmost Longitudinal Valley, eastern Taiwan: Structural development of a vanishing suture. *Tectonophysics*, **692**, 295-308, doi: 10.1016/j.tecto.2015.12.026. [[Link](#)]
- Shyu, J. B. H., Y. R. Chuang, Y. L. Chen, Y. R. Lee, and C. T. Cheng, 2016b: A new on-land seismogenic structure source database from the Taiwan Earthquake Model (TEM) project for seismic hazard analysis of Taiwan. *Terr. Atmos. Ocean. Sci.*, **27**, 311-323, doi: 10.3319/TAO.2015.11.27.02(TEM). [[Link](#)]
- Suppe, J., 1984: Kinematics of arc-continent collision, flipping of subduction, and back-arc spreading near Taiwan. *Mem. Geol. Soc. China*, **6**, 21-33.
- Sylvester, A. G., 1988: Strike-slip faults. *GSA Bull.*, **100**, 1666-1703, doi: 10.1130/0016-7606(1988)100<1666:SSF>2.3.CO;2. [[Link](#)]
- Tchalenko, J. S., 1970: Similarities between Shear Zones of Different Magnitudes. *Geol. Soc. Am. Bull.*, **81**, 1625-1640, doi: 10.1130/0016-7606(1970)81[1625:SBSZO D]2.0.CO;2. [[Link](#)]
- Wakabayashi, J., J. V. Hengesh, and T. L. Sawyer, 2004: Four-dimensional transform fault processes: Progressive evolution of step-overs and bends. *Tectonophysics*, **392**, 279-301, doi: 10.1016/j.tecto.2004.04.013. [[Link](#)]
- Westaway, R., 1995: Deformation around stepovers in strike-slip fault zones. *J. Struct. Geol.*, **17**, 831-846, doi: 10.1016/0191-8141(94)00098-K. [[Link](#)]
- Yamaguchi, M. and Y. Ota, 2004: Tectonic interpretations of Holocene marine terraces, east coast of Coastal Range, Taiwan. *Quat. Int.*, **115-116**, 71-81, doi: 10.1016/S1040-6182(03)00097-1. [[Link](#)]
- Yang, Y.-C., 1953: Earthquakes in Hualien in the latest 41 years. *Hualien Literatures*, **1**, 67-71. (in Chinese)
- Yang, Y.-H., J.-C. Hu, H. Tung, M.-C. Tsai, Q. Chen, Q. Xu, Y.-J. Zhang, J.-J. Zhao, G.-X. Liu, J.-N. Xiong, J.-Y. Wang, B. Yu, C.-Y. Chiu, and Z. Su, 2018: Co-Seismic and Postseismic Fault Models of the 2018 Mw 6.4 Hualien Earthquake Occurred in the Junction of Collision and Subduction Boundaries Offshore Eastern Taiwan. *Remote Sens.*, **10**, 1372, doi: 10.3390/rs10091372. [[Link](#)]
- Yen, J.-Y., C.-H. Lu, C.-P. Chang, A. J. Hooper, Y.-H. Chang, W.-T. Liang, T.-Y. Chang, M.-S. Lin, and K.-S. Chen, 2011: Investigating active deformation in the northern Longitudinal Valley and City of Hualien in eastern Taiwan using persistent scatterer and small-baseline SAR interferometry. *Terr. Atmos. Ocean. Sci.*, **22**, 291-304, doi: 10.3319/TAO.2010.10.25.01(TT). [[Link](#)]
- Yen, J.-Y., C.-H. Lu, R. J. Dorsey, H. Kuo-Chen, C.-P. Chang, C.-C. Wang, R. Y. Chuang, Y.-T. Kuo, C.-Y. Chiu, Y.-H. Chang, F. Bovenga, and W.-Y. Chang, 2018: Insights into seismogenic deformation during the 2018 Hualien, Taiwan, earthquake sequence from InSAR, GPS, and modeling. *Seismol. Res. Lett.*, **90**, 78-87, doi: 10.1785/0220180228. [[Link](#)]